

8 Quantum Cluster Methods

Erik Koch

Computational Materials Science

German Research School for Simulation Sciences

Jülich

Contents

1	Periodic systems	4
1.1	Lattices	4
1.2	Superlattices	8
2	Variational methods	10
2.1	Variational Monte Carlo	14
2.2	Correlated sampling	16
2.3	Gutzwiller approximation	18
2.4	Brinkman-Rice transition	20
3	Projection techniques	23
3.1	Importance sampling	24
3.2	Fixed-node Monte Carlo	25
3.3	Optimization of the trial function	26
3.4	Quasi-particle energies	30
4	Conclusion	35

The central challenge of electronic structure theory is the solution of the many-electron Hamiltonian in the Born-Oppenheimer approximation (in atomic units)

$$H = -\frac{1}{2} \sum_i \vec{\nabla}_i^2 + \sum_i V_{\text{ext}}(\vec{r}_i) + \sum_{i < j} \frac{1}{|\vec{r}_i - \vec{r}_j|}, \quad (1)$$

where the external potential is, e.g., the Coulomb potential of the nuclei of charge Z_I at position \vec{R}_I , shifted by their mutual Coulomb interaction

$$V_{\text{ext}}(\vec{r}) = \sum_I \frac{Z_I}{|\vec{r} - \vec{R}_I|} + \sum_{I < J} \frac{Z_I Z_J}{|\vec{R}_I - \vec{R}_J|}. \quad (2)$$

Introducing a basis-set $\{\varphi_\alpha(x)\}$ of spin-orbitals, we can rewrite H in second quantization

$$H = - \sum_{\alpha\beta} t_{\alpha\beta} c_\alpha^\dagger c_\beta + \frac{1}{2} \sum_{\alpha\beta\gamma\delta} U_{\alpha\delta} c_\alpha^\dagger c_\beta^\dagger c_\gamma c_\delta \quad (3)$$

where the creation/annihilation operators fulfill the anticommutation relations $\{c_\alpha^\dagger, c_\beta^\dagger\} = 0 = \{c_\alpha, c_\beta\}$ and $\{c_\alpha, c_\beta^\dagger\} = \langle\alpha|\beta\rangle = S_{\alpha\beta}$, and S is the overlap matrix [1]. The matrix elements are given by integrating over the orbital degrees of freedom $x = (\vec{r}, \sigma)$

$$t_{\alpha\beta} = \sum_{\alpha'\beta'} (S^{-1})_{\alpha\alpha'} \int dx \overline{\varphi_{\alpha'}(x)} \left(\frac{1}{2} \vec{\nabla}^2 - V_{\text{ext}}(\vec{r}) \right) \varphi_{\beta'}(x) (S^{-1})_{\beta'\beta} \quad (4)$$

and

$$U_{\alpha\delta} = \sum_{\substack{\alpha'\delta' \\ \beta'\gamma'}} S_{\alpha\alpha'}^{-1} S_{\beta\beta'}^{-1} \int dx \int dx' \overline{\varphi_{\alpha'}(x)} \overline{\varphi_{\beta'}(x')} \frac{1}{|\vec{r} - \vec{r}'|} \varphi_{\gamma'}(x') \varphi_{\delta'}(x) S_{\gamma'\gamma}^{-1} S_{\delta'\delta}^{-1}. \quad (5)$$

This representation of the Hamiltonian is suited for introducing approximations. By truncating the basis-set to only K functions, the Hilbert space \mathcal{H} of H for a system with N electrons is restricted to a finite variational subspace $\mathcal{H}(\{\varphi_{\alpha_n}(x); |n = 1 \dots K\})$ of dimension $\binom{K}{N}$. Working with a finite basis set introduces a basis-set error. To keep it small, the basis functions are chosen such that the eigenstates of interest are represented well on $\mathcal{H}(\{\varphi_{\alpha_n}(x) | n = 1 \dots K\})$, using, e.g., low-energy orbitals to represent the ground state. The basis-set error can be estimated by comparing results calculated with basis sets of increasing size and extrapolating to the complete-basis-set-limit. Such calculations are computationally demanding, as the dimension of the Hilbert space increases for $K \gg N \gg 1$ (using Stirling's approximation) with a high power, given by the (fixed) number of electrons in the system, as $\mathcal{O}(K^N)$.

For extended systems the problem becomes even harder. To ensure size-consistency [2], meaning that the basis-set error for extensive observables, e.g., the total energy, scales at most with the number of electrons, we have to increase K along with N , leading to an exponential scaling of the variational space with system size. Practical simulations are therefore restricted to quite small clusters. These have a large fraction of surface atoms. As a simple example, for a $10 \times 10 \times 10$ cluster 488 of the 1000 atoms are on the surface. The surface effects can be

removed by putting the system in a simulation cell spanned by three vectors \vec{R}_i and assuming that the system is periodically repeated [3]. Instead of leaving the system, an electron passing through a face of the simulation cell continues into the neighboring cell, while one of its images enters through the opposite face. Thus, we are dealing with an extended system with an infinite number of electrons. Still, by virtue of the periodicity, only the N electrons inside the simulation cell are independent degrees of freedom. We can then restrict the calculation to the simulation cell $\mathcal{C} = \{ \sum_i x_i \vec{R}_i \mid x_i \in [0, 1) \}$ by including the periodic images of the external potential (created inside the simulation cell) and the interaction with the electrons outside the simulation box in the Hamiltonian [4]

$$H_{\text{pbc}} = -\frac{1}{2} \sum_{i=1}^N \vec{\nabla}_i^2 + \sum_{\vec{n} \in \mathbb{Z}^3} \sum_i V_{\text{ext}}^{\mathcal{C}}(\vec{r}_i - \vec{R}_{\vec{n}}) + \frac{1}{2} \sum_{\vec{n} \in \mathbb{Z}^3} \sum_{i,j}' \frac{1}{|\vec{r}_i - \vec{r}_j - \vec{R}_{\vec{n}}|}. \quad (6)$$

where $\vec{R}_{\vec{n}} = \sum_{i=1}^3 n_i \vec{R}_i$ and the prime on the last sum indicates that $i \neq j$ when $\vec{n} = 0$. The eigenfunctions of (6) on the simulation cell \mathcal{C} represent a system of average electron density $N/V_{\mathcal{C}}$. We see that, while removing surface effects, the introduction of periodic boundary conditions not only modifies interactions of ranges longer than the radius of the simulation cell but also suppress fluctuations of the number of electrons between simulation cells. Moreover, the average electron density can only be a multiple of $1/V_{\mathcal{C}}$ as the simulation cell must contain an integer number of electrons. Obviously, these finite-size errors vanish in the limit of infinite simulation cell volume $V_{\mathcal{C}} \rightarrow \infty$. Fig. 1 shows a comparison of the finite-size scaling for the ground-state energy with open and with periodic boundary conditions. For systems that develop long-range correlations, care has to be taken in the finite-size extrapolation for correlation functions $C(\vec{r}, \vec{r}')$, as imposing periodic boundary conditions $C(\vec{r}, \vec{r} + \vec{R}_i) = C(\vec{r}, \vec{r}')$ can frustrate correlations that are not commensurate with the simulation cell. This becomes particularly evident for a crystal in which the external potential of the infinite system is periodic $V_{\text{ext}}(\vec{r} + \vec{a}_i) = V_{\text{ext}}(\vec{r})$ with the periodicity of the lattice spanned by the vectors \vec{a}_i . Only when the vectors \vec{R}_i spanning \mathcal{C} are chosen as integer linear combinations $\vec{R}_i = \sum_j n_{ij} \vec{a}_j$ will the external potential in H_{pbc} agree with V_{ext} :

$$\sum_{\vec{n} \in \mathbb{Z}^3} V_{\text{ext}}^{\mathcal{C}}(\vec{r} - \vec{R}_{\vec{n}}) = V_{\text{ext}}(\vec{r}), \quad (7)$$

where $V_{\text{ext}}^{\mathcal{C}}$ is the external potential originating, e.g., from the nuclei inside \mathcal{C} .

For such periodic systems the nature of the many-body problem becomes apparent. The interaction term by itself is not particularly complicated. It is diagonal in real space, so finding the arrangement of electrons that minimizes their mutual Coulomb repulsion is a straightforward classical optimization problem, the solution being a Wigner crystal [5]. The kinetic energy, on the other hand, is diagonal in k -space. For a lattice-periodic potential, V_{ext} couples only a discrete set of k -vectors, so that the single-electron part of H can be solved in terms of Bloch waves. Solutions of the full problem thus have to balance the extended Bloch waves (kinetic energy) against the localized Wigner crystal (electron-electron repulsion).

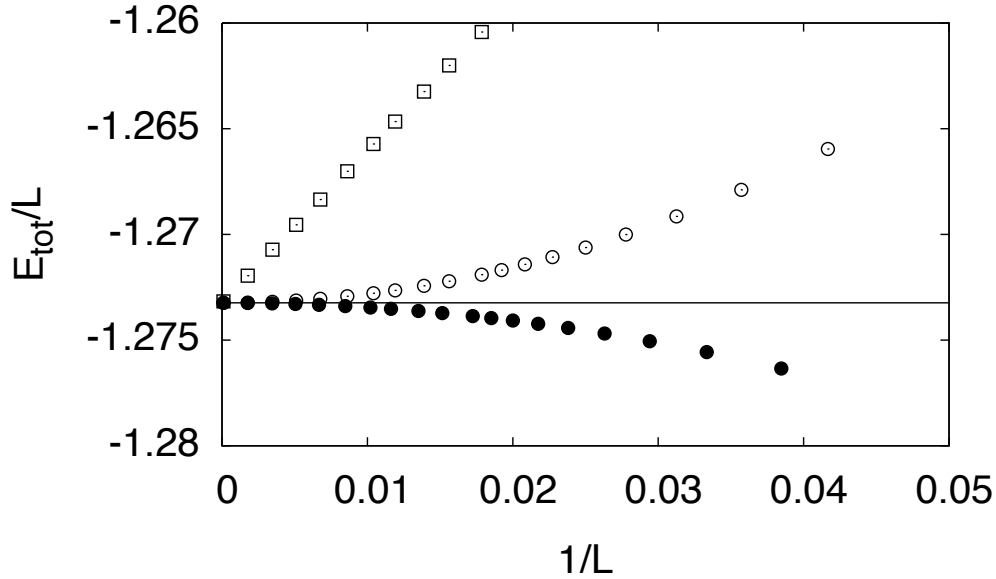


Fig. 1: Energy per site for Hubbard chains of L sites with open and periodic boundary conditions. Calculations are for the non-interacting half-filled Hubbard model with nearest-neighbor hopping t . For open boundary conditions (open squares) the energy converges linearly with $1/L$ to the result for the infinite chain, $\varepsilon_\infty = -4t/\pi$. For periodic boundary conditions (circles) convergence is quadratic, both for open- and closed-shell chains.

1 Periodic systems

1.1 Lattices

A d -dimensional lattice is the collection of points

$$\mathcal{L} = \left\{ \mathbf{r}_{n_1, \dots, n_d} = \sum_i n_i \mathbf{a}_i \mid n_i \in \mathbb{Z} \right\} \quad (8)$$

defined by the integer linear combinations of a set of d linearly independent vectors \mathbf{a}_i . Arranging the vectors \mathbf{a}_i into a matrix $\mathbf{A} = (\mathbf{a}_1, \mathbf{a}_2, \dots)$, we see that the points in the lattice are given by $\mathbf{r}_n = \mathbf{A}\mathbf{n}$ with $\mathbf{n} \in \mathbb{Z}^d$; i.e., \mathbf{A} maps the d -dimensional cubic lattice into \mathcal{L} . Likewise, we can write an arbitrary point $\mathbf{r} = \mathbf{A}\mathbf{f}$. In general, the coordinates $\mathbf{f} = \mathbf{A}^{-1}\mathbf{r}$ in the basis \mathbf{A} will not be integers. They are called the fractional coordinates of \mathbf{r} . The primitive cell defined by \mathbf{A} is the set of all points \mathbf{r} whose fractional coordinates lie in the unit cube $\mathbf{f} \in [0, 1)^d$. Its volume is $V_c = |\det(\mathbf{A})|$. It is convenient to arrange the vectors \mathbf{a}_i such that the determinant is positive. The vectors \mathbf{a}_i are called the primitive vectors of the lattice \mathcal{L} . They are not unique: we can construct an equivalent set of primitive vectors $\tilde{\mathbf{A}}$ by adding to $\pm\mathbf{a}_i$ any integer multiple of the other $\mathbf{a}_{j \neq i}$, such that $|\det(\tilde{\mathbf{A}})| = |\det(\mathbf{A})|$. Since the transformation $\tilde{\mathbf{A}} = \mathbf{A}\mathbf{M}$ is then given by an integer matrix \mathbf{M} with $|\det(\mathbf{M})| = 1$, by Cramer's rule, its inverse is also an integer matrix. Thus any point in the lattice \mathcal{L} can be written in terms of either set of primitive vectors: $\mathbf{A}\mathbf{n} = \tilde{\mathbf{A}}\tilde{\mathbf{n}}$, with the integer indices related by $\tilde{\mathbf{n}} = \mathbf{M}^{-1}\mathbf{n}$. The canonical choice is to make the primitive vectors as short as possible, $\tilde{\mathbf{a}}_i = \sum_{j \neq i} \text{round}(\mathbf{a}_i \cdot \mathbf{a}_j / \|\mathbf{a}_j\|^2) \mathbf{a}_j$, so they provide the notion of nearest-neighbor and give a compact unit cell.

The reciprocal lattice $\mathcal{R}_{\mathcal{L}}$ associated with \mathcal{L} arises naturally when considering the Fourier transform of lattice periodic functions, i.e., functions $V(\mathbf{r} + \mathbf{A}\mathbf{n}) = V(\mathbf{r})$. The Fourier expansion of a general function $V(\mathbf{r})$ is given by

$$V(\mathbf{r}) = \int d^d k \hat{V}(\mathbf{k}) e^{i\mathbf{k}\cdot\mathbf{r}}. \quad (9)$$

When $V(\mathbf{r})$ is periodic on \mathcal{L} , we have

$$V(\mathbf{r} + \mathbf{A}\mathbf{n}) = \int d^d k \hat{V}(\mathbf{k}) e^{i\mathbf{k}\cdot\mathbf{r}} e^{i\mathbf{k}\cdot\mathbf{A}\mathbf{n}} = V(\mathbf{r}). \quad (10)$$

By the linear independence of Fourier modes it follows that only terms with $\exp(i\mathbf{k} \cdot \mathbf{A}\mathbf{n}) = 1$ for all $\mathbf{n} \in \mathbb{Z}^d$ can contribute. The k -vectors fulfilling this condition form the reciprocal lattice

$$\mathcal{R}_{\mathcal{L}} = \left\{ \mathbf{G}\mathbf{m} \mid \mathbf{m} \in \mathbb{Z}^d \right\} \quad (11)$$

with primitive vectors $\mathbf{G} = (2\pi\mathbf{A}^{-1})^T$. Since $(2\pi\mathbf{G}^{-1})^T = \mathbf{A}$, the reciprocal lattice of $\mathcal{R}_{\mathcal{L}}$ is \mathcal{L} . By construction, the reciprocal lattice vectors $\mathbf{g} \in \mathcal{R}_{\mathcal{L}}$ define plane waves $\exp(i\mathbf{g} \cdot \mathbf{r})$ for which all lattice points $\mathbf{r}_{\mathbf{n}} \in \mathcal{L}$ fall on planes of phase = 1. The reciprocal lattice vectors, except the gamma-point $\mathbf{g} = \mathbf{0}$, are thus orthogonal to planes containing an infinite number of lattice points. A given set of lattice planes can be characterized by the shortest reciprocal lattice vector $\mathbf{g}_{\min} = \mathbf{G}\mathbf{m}$ perpendicular to it. The expansion coefficients \mathbf{m} in terms of the primitive reciprocal vectors are the Miller indices. As for the real lattice, the primitive vectors are not unique: $\tilde{\mathbf{A}} = \mathbf{A}\mathbf{M}$ gives $\tilde{\mathbf{G}} = (2\pi\tilde{\mathbf{A}}^{-1})^T = \mathbf{G}(\mathbf{M}^{-1})^T$, which also span $\mathcal{R}_{\mathcal{L}}$. The canonical choice for the primitive reciprocal cell is $\mathbf{k} \in \mathbf{G}(-1/2, 1/2]^d$. A momentum \mathbf{k} from a primitive reciprocal cell (first Brillouin zone) is called a crystal momentum.

Transforming the single-electron Hamiltonian

$$H_{\text{single}} = -\frac{1}{2} \nabla_{\mathbf{r}}^2 + V_{\text{ext}}(\mathbf{r}) \quad (12)$$

with lattice-periodic potential $V_{\text{ext}}(\mathbf{r}) = \sum_{\mathbf{m} \in \mathbb{Z}^d} \hat{V}_{\mathbf{G}\mathbf{m}} e^{i\mathbf{G}\mathbf{m}\cdot\mathbf{r}}$ to k -space

$$\langle \mathbf{k} | H_{\text{single}} | \mathbf{k}' \rangle = \frac{\mathbf{k}^2}{2} \delta(\mathbf{k} - \mathbf{k}') + \hat{V}_{\mathbf{G}\mathbf{m}} \delta(\mathbf{k} - \mathbf{k}' - \mathbf{G}\mathbf{m}) \quad (13)$$

or, more elegantly,

$$H_{\text{single}} = \sum_{\mathbf{k}} \frac{\mathbf{k}^2}{2} c_{\mathbf{k},\sigma}^\dagger c_{\mathbf{k},\sigma} + \sum_{\mathbf{k}} \sum_{\mathbf{m} \in \mathbb{Z}^d} \hat{V}_{\mathbf{G}\mathbf{m}} c_{\mathbf{k}+\mathbf{G}\mathbf{m},\sigma}^\dagger c_{\mathbf{k},\sigma}, \quad (14)$$

we see that the Hamiltonian only couples states whose wave-vectors differ by reciprocal lattice vectors (for $\mathbf{m} \neq \mathbf{0}$ they are Umklapp processes). Thus, H_{single} is block-diagonal in k -space so that its eigenstates are of the form

$$\varphi_{n,\mathbf{k}}(\mathbf{r}) = \sum_{\mathbf{m} \in \mathbb{Z}^d} c_{n,\mathbf{m}} e^{i(\mathbf{k}+\mathbf{G}\mathbf{m})\cdot\mathbf{r}}, \quad (15)$$

where \mathbf{k} , now restricted to the primitive reciprocal cell, is the crystal momentum of the state and n its band index. Under translations by a lattice vector $\mathbf{A}\mathbf{n}$ they transform as

$$\varphi_{n,\mathbf{k}}(\mathbf{r} + \mathbf{A}\mathbf{n}) = e^{i\mathbf{k}\cdot\mathbf{A}\mathbf{n}} \varphi_{n,\mathbf{k}}(\mathbf{r}), \quad (16)$$

i.e., as irreducible representations of the abelian translation group. This is the Bloch theorem. Transforming back to real space, we could determine the eigenfunctions $\varphi_{n,\mathbf{k}}(\mathbf{r})$ by solving the eigenvalue problem for H_{single}

$$\left(\frac{1}{2} \nabla_{\mathbf{r}}^2 + V_{\text{ext}}(\mathbf{r}) \right) \varphi_{n,\mathbf{k}}(\mathbf{r}) = \varepsilon_{n,\mathbf{k}} \varphi_{n,\mathbf{k}}(\mathbf{r}) \quad (17)$$

not on the entire space \mathbb{R}^d , but on a single primitive lattice cell imposing \mathbf{k} -boundary conditions $\varphi_{n,\mathbf{k}}(\mathbf{a}_i) = e^{i\mathbf{k}\cdot\mathbf{a}_i} \varphi_{n,\mathbf{k}}(\mathbf{0})$. It is, however, more common to rewrite (15) as

$$\varphi_{n,\mathbf{k}}(\mathbf{r}) = e^{i\mathbf{k}\cdot\mathbf{r}} \sum_{\mathbf{m}} c_{n,\mathbf{m}} e^{i\mathbf{G}\mathbf{m}\cdot\mathbf{r}} = e^{i\mathbf{k}\cdot\mathbf{r}} u_{n,\mathbf{k}}(\mathbf{r}). \quad (18)$$

with the lattice-periodic Bloch function $u_{n,\mathbf{k}}(\mathbf{r})$. Using this form as an ansatz in (17), we see that the Bloch functions can be obtained from the eigenvalue problem

$$\left(\frac{1}{2} (-i\nabla_{\mathbf{r}} + \mathbf{k})^2 + V(\mathbf{r}) \right) u_{n,\mathbf{k}}(\mathbf{r}) = \varepsilon_{n,\mathbf{k}} u_{n,\mathbf{k}}(\mathbf{r}), \quad (19)$$

on a primitive cell of \mathcal{L} with periodic boundary conditions. We note that in this equation \mathbf{k} plays the role of a constant vector potential.

For a general time-reversal-symmetric Hamiltonian, every eigenfunction $\varphi_{\alpha}(\mathbf{r})$ is degenerate with its complex conjugate, so that we can choose real eigenfunctions. Taking the complex conjugate of (19) shows that for a real potential we can choose $\overline{u_{n,\mathbf{k}}(\mathbf{r})} = u_{n,-\mathbf{k}}(\mathbf{r})$. When the potential is inversion-symmetric, $V(-\mathbf{r}) = V(\mathbf{r})$, then $\varphi_{\alpha}(-\mathbf{r})$ is degenerate with $\varphi_{\alpha}(\mathbf{r})$. For (19) it implies $u_{n,\mathbf{k}}(-\mathbf{r}) = u_{n,-\mathbf{k}}(\mathbf{r})$. In the presence of both symmetries we obtain $\overline{u_{n,\mathbf{k}}(\mathbf{r})} = u_{n,-\mathbf{k}}(\mathbf{r}) = u_{n,\mathbf{k}}(-\mathbf{r})$.

A Bloch theorem also holds for the eigenstates of a many-body Hamiltonian that is invariant under lattice translations. Translating *all* electrons by the *same* lattice vector $\mathbf{A}\mathbf{n}$ will multiply the wave-function by a phase $e^{i\mathbf{k}_{\text{tot}}\cdot\mathbf{A}\mathbf{n}}$, where \mathbf{k}_{tot} is the *total* crystal momentum of the many-body state. Thus, in k -space the Hamiltonian block-diagonalizes into sectors with a given total crystal momentum. Writing H in k -space

$$H = \sum_{\mathbf{k},\sigma} \left(\frac{\mathbf{k}^2}{2} c_{\mathbf{k},\sigma}^{\dagger} c_{\mathbf{k},\sigma} + \sum_{\mathbf{m}} \hat{V}_{\mathbf{G}\mathbf{m}} c_{\mathbf{k}+\mathbf{G}\mathbf{m},\sigma}^{\dagger} c_{\mathbf{k},\sigma} + \frac{1}{2} \sum_{\mathbf{k}',\sigma';\mathbf{q}} c_{\mathbf{k}+\mathbf{q},\sigma}^{\dagger} c_{\mathbf{k}'-\mathbf{q},\sigma'}^{\dagger} \frac{1}{|\mathbf{q}|^2} c_{\mathbf{k}',\sigma'} c_{\mathbf{k},\sigma} \right) \quad (20)$$

we see that acting on a Slater determinant of plane waves with momenta \mathbf{k}_i (or Bloch waves of crystal momenta \mathbf{k}_i), the Hamiltonian does not change total crystal momentum $\mathbf{k}_{\text{tot}} = \sum \mathbf{k}_i$. However, while the kinetic energy is diagonal and the external potential scatters only between plane waves differing by a reciprocal lattice vector, the electron-electron interaction scatters

plane waves of arbitrary single-electron momentum. Thus, for the eigenvalue problem we have to consider Slater determinants of plane waves with arbitrary wave-vectors \mathbf{k}_i .

As the simplest example, let us consider the Slater determinant of two plane waves

$$\Phi_{\mathbf{k}_1, \mathbf{k}_2}(\mathbf{r}_1, \mathbf{r}_2) = \frac{1}{\sqrt{2}} \left(\frac{1}{(2\pi)^{d/2}} \right)^2 \begin{vmatrix} e^{i\mathbf{k}_1 \cdot \mathbf{r}_1} & e^{i\mathbf{k}_2 \cdot \mathbf{r}_1} \\ e^{i\mathbf{k}_1 \cdot \mathbf{r}_2} & e^{i\mathbf{k}_2 \cdot \mathbf{r}_2} \end{vmatrix} \propto e^{i(\mathbf{k}_1 \cdot \mathbf{r}_1 + \mathbf{k}_2 \cdot \mathbf{r}_2)} - e^{i(\mathbf{k}_2 \cdot \mathbf{r}_1 + \mathbf{k}_1 \cdot \mathbf{r}_2)} \quad (21)$$

By construction it transforms as desired under a shift of *all* electrons by a lattice vector

$$\Phi_{\mathbf{k}_1, \mathbf{k}_2}(\mathbf{r}_1 + \mathbf{A}\mathbf{n}, \mathbf{r}_2 + \mathbf{A}\mathbf{n}) = e^{i(\mathbf{k}_1 + \mathbf{k}_2) \cdot \mathbf{A}\mathbf{n}} \Phi_{\mathbf{k}_1, \mathbf{k}_2}(\mathbf{r}_1, \mathbf{r}_2). \quad (22)$$

The situation is, however, markedly different from the single-electron case (15): there, we can always translate a single electron coordinate into a primitive cell, allowing us to consider the single-electron Bloch functions on a finite volume. For more electrons, however, their relative distance is unchanged under the collective translation, so that we cannot bring all coordinates into a finite volume. To make this possible, we would need a Bloch-type theorem for translations of *individual* electrons:

$$\Phi_{\mathbf{k}_1, \mathbf{k}_2}(\mathbf{r}_1 + \mathbf{c}, \mathbf{r}_2) = e^{i\tilde{\mathbf{k}} \cdot \mathbf{c}} \Phi_{\mathbf{k}_1, \mathbf{k}_2}(\mathbf{r}_1, \mathbf{r}_2) \quad (23)$$

(the equivalent equation for translations of \mathbf{r}_2 follows from the antisymmetry). Inserting (21) we see that such an individual-electron Bloch-condition puts constraints on the allowed momenta: $\exp(i(\mathbf{k}_i - \tilde{\mathbf{k}}) \cdot \mathbf{c}) = 1$. Thus, to be able to restrict the many-electron wavefunction to a primitive cell spanned by three vectors \mathbf{C} with boundary conditions

$$\Phi_{\mathbf{k}_1, \mathbf{k}_2}(\mathbf{c}_i, \mathbf{r}_2, \dots) = e^{i\tilde{\mathbf{k}} \cdot \mathbf{c}_i} \Phi_{\mathbf{k}_1, \mathbf{k}_2}(\mathbf{0}, \mathbf{r}_2, \dots), \quad (24)$$

we can only allow Slater determinants constructed from plane waves with wave vectors \mathbf{k}_i such that the $\mathbf{k}_i - \tilde{\mathbf{k}}$ are reciprocal lattice vectors of \mathbf{C} . For $\tilde{\mathbf{k}} = \mathbf{0}$ we obtain the simulation cell with periodic boundary conditions discussed in the introduction. The eigenfunctions of H with boundary conditions (24) can be written in the Bloch-like form

$$\Psi_{n, \tilde{\mathbf{k}}}^{\mathbf{C}}(\mathbf{r}_1, \mathbf{r}_2, \dots) = e^{i\tilde{\mathbf{k}} \cdot \sum_i \mathbf{r}_i} U_{n, \tilde{\mathbf{k}}}^{\mathbf{C}}(\mathbf{r}_1, \mathbf{r}_2, \dots), \quad (25)$$

where $U_{n, \tilde{\mathbf{k}}}^{\mathbf{C}}(\mathbf{r}_1, \mathbf{r}_2, \dots)$ is invariant under translations of a single electron by a vector from \mathbf{C} and antisymmetric under particle exchange. While $U_{n, \tilde{\mathbf{k}}}^{\mathbf{C}}$ apparently is the many-body generalization of the single-electron Bloch function $u_{n, \mathbf{k}}(\mathbf{r})$, we have to keep in mind that its construction is based on the artificial boundary conditions (24), which depend on the choice of the volume \mathbf{C} . When the volume is chosen small, calculations are simple but the wave functions $\Psi_{n, \tilde{\mathbf{k}}}^{\mathbf{C}}$ will give poor approximations to the actual ground state, while increasing the cell improves the accuracy but also makes calculations increasingly difficult.

Physically, as in the single-electron case (19), the twisted boundary conditions (24) correspond to a constant vector potential. The dependence of the ground state energy $E_0^{\mathbf{C}}(\tilde{\mathbf{k}})$ can be used to distinguish metallic from (Mott) insulating systems: the second derivative at $\tilde{\mathbf{k}} = \mathbf{0}$ of the energy with respect to the current driving vector potential gives the static response. For metals it stays finite while for insulators it vanishes in the thermodynamic limit [6].

1.2 Superlattices

For a system with lattice periodicity the single- and many-electron boundary conditions (16) and (24) should be consistent. This implies, in particular, that the vectors spanning the cell should be integer linear-combinations of the primitive lattice vectors, $\mathbf{c}_i = \sum \mathbf{a}_j l_{ij}$, or, in matrix notation, $\mathbf{C} = \mathbf{A}\mathbf{L}$, where the columns of \mathbf{L} are the primitive cell vectors in units of the primitive lattice vectors. The vectors \mathbf{C} span a lattice $\mathcal{S} \subseteq \mathcal{L}$, called a superlattice. The volume of the primitive unit cell of \mathbf{C} is $|\det(\mathbf{L})|$ times the volume of the primitive lattice cell. Since \mathbf{L} is an integer matrix, its determinant is also an integer.

As the choice of the primitive lattice vectors \mathbf{A} for a given lattice \mathcal{L} is not unique, so is the choice of \mathbf{L} for a given superlattice \mathcal{S} . We can, however, easily check whether, for given primitive lattice vectors \mathbf{A} , two integer matrices span the same superlattice by reducing them to their Hermite normal form [7] and checking if they agree. The reduction of a non-singular integer matrix \mathbf{L} to its *Hermite normal form* (HNF)

$$\mathbf{A} = \begin{pmatrix} \lambda_{11} & 0 & 0 & \cdots \\ \lambda_{21} & \lambda_{22} & 0 & \\ \lambda_{31} & \lambda_{32} & \lambda_{33} & \\ \vdots & & & \ddots \end{pmatrix} \quad (26)$$

with $\lambda_{ii} \geq 1$, and $\lambda_{ii} > \lambda_{ij} \geq 0$ can be done recursively. Allowed operations that leave the superlattice spanned by the transformed matrix unchanged are (i) multiplying a column by ± 1 , (ii) exchanging columns, and (iii) adding an integer multiple of another column. The reduction algorithm [8] is based on the Euclidean algorithm for finding the greatest common divisor

$$\gcd(a, b) = \begin{cases} |a| & \text{if } b = 0 \quad (\text{operation of type (i)}) \\ \gcd(b, a) & \text{if } |a| < |b| \quad (\text{operation of type (ii)}) \\ \gcd(a - \lfloor a/b \rfloor b, b) & \text{otherwise} \quad (\text{operation of type (iii)}) \end{cases} \quad (27)$$

where a and b are the matrix elements in a given row of the matrix, and we perform the operations not just on these matrix elements but on their entire column vectors. To reduce the first row of \mathbf{L} to the required form, we apply the Euclidean algorithm on the last two columns, reducing the coefficient in the last column to zero. In this way we reduce all matrix elements except the first to zero, obtaining $\lambda_{11} = \gcd(l_{11}, \dots, l_{1d})$. We iterate this procedure for the submatrix obtained by removing the first row and column to bring the matrix to lower triangular form. Finally, we use column operations to replace the off-diagonal elements in a row by their remainders on division by the corresponding diagonal element.

Besides giving a criterion for determining equivalent primitive cell vectors, the Hermite normal form gives a prescription for enumerating all non-equivalent periodic clusters of a given size. We have to be careful, however, when the lattice \mathcal{L} spanned by \mathbf{A} has point symmetries besides simple inversion. Since the construction of \mathbf{A} contains no information on the underlying lattice, such additional symmetries can render superlattices with different HNF equivalent.

Fig. 2 gives an example of how different equivalent primitive cells can appear. For the square lattice with point-symmetry C_{4v} , we see that primitive vectors spanning the same superlattice

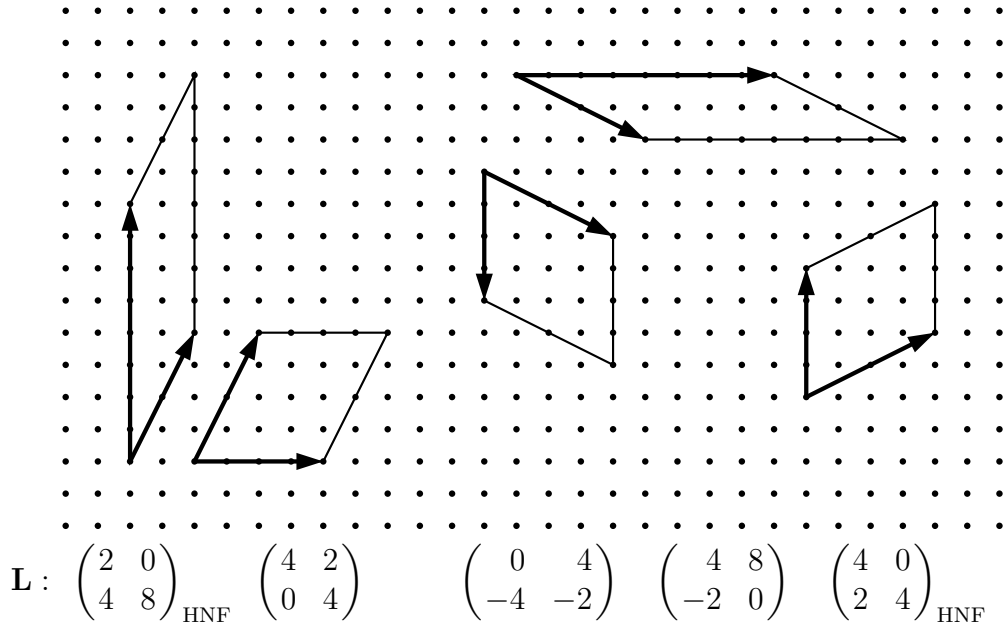


Fig. 2: Primitive superlattice cells on a square lattice. All primitive superlattice vectors span the same superlattice, i.e., calculations for any of the shown cells will give the same results. The primitive superlattice vectors \mathbf{L} are shown below the plot. The first two plots show a set of primitive vectors and the corresponding Hermite normal form. The next two are obtained by rotating the vectors by $-\pi/2$, $(x, y) \rightarrow (-y, x)$. Because of the point-symmetry of the underlying square lattice, they span equivalent superlattices. Their Hermite normal form, shown on the far right, is, however, different from the unrotated HNF on the far left.

can have different Hermite normal form when they are related by a non-trivial point-symmetry operation. This happens when the primitive cells break the point symmetry of the lattice. It is often advantageous to work with cells that retain symmetries of the underlying lattice. Well known examples are the conventional cells of cubic lattices, e.g., the face-centered cubic lattice

$$\mathbf{A} = \frac{a}{2} \begin{pmatrix} 0 & 1 & 1 \\ 1 & 0 & 1 \\ 1 & 1 & 0 \end{pmatrix} \quad \mathbf{C} = a \begin{pmatrix} 1 & 0 & 0 \\ 0 & 1 & 0 \\ 0 & 0 & 1 \end{pmatrix} \quad \mathbf{L} = \begin{pmatrix} -1 & 1 & 1 \\ 1 & -1 & 1 \\ 1 & 1 & -1 \end{pmatrix}. \quad (28)$$

While the primitive lattice vectors \mathbf{A} do not exhibit the cubic symmetry of the lattice, the vectors of the conventional unit cell \mathbf{C} do. Symmetry is one of the criteria used for selecting cells that best represent the infinite system [9].

The reciprocal lattice \mathcal{R}_S of S is spanned by the primitive vectors $\mathbf{K}_s = (2\pi\mathbf{C}^{-1})^T$. They can be written in terms of the reciprocal lattice vectors of \mathcal{L} as

$$\mathbf{K}_s = (2\pi\mathbf{C}^{-1})^T = \mathbf{K} (\mathbf{L}^{-1})^T \quad (29)$$

The primitive cell spanned by \mathbf{K}_s is smaller than that spanned by \mathbf{K} by a factor of $1/|\det(\mathbf{L})|$. The Slater determinants in a simulation on the primitive cell spanned by \mathbf{C} with periodic boundary conditions can then contain Bloch waves of wave vector $\mathbf{k} = \mathbf{K}_s \mathbf{m}$ with $\mathbf{m} \in \mathbb{Z}^d$ that fall in the Brillouin zone of the original lattice. With twisted boundary conditions (24), the allowed

wave vectors are shifted by $\tilde{\mathbf{k}}$. The choice $\tilde{\mathbf{k}} = \mathbf{k}_i/2$ corresponds to a sign-change under a translation by \mathbf{c}_i , i.e., antiperiodic boundary conditions in that direction.

When the primitive superlattice vectors are chosen as integer multiples of the primitive lattice vectors, $\mathbf{c}_i = n_i \mathbf{a}_i$, the reciprocal lattice shifted by $\tilde{\mathbf{k}} = \sum_i (n_i - 1) \mathbf{k}_i / 2n_i$ forms a Monkhorst-Pack grid of special k -points that are popular for Brillouin-zone integrations [10].

2 Variational methods

Conceptually, the variational approach is straightforward: to find the ground state of a Hamiltonian H , just minimize the energy expectation value

$$E[\Psi] = \frac{\langle \Psi | H | \Psi \rangle}{\langle \Psi | \Psi \rangle}. \quad (30)$$

The practical problem is, of course, the choice of a suitable variational space. The systematic approach is to write the trial wave function as a linear combination of Slater determinants $\Psi(\mathbf{r}) = \sum_{\alpha} c_{\alpha} \Phi_{\alpha}(\mathbf{r})$ and allow all amplitudes c_{α} to vary. For a finite system with N electrons and a finite basis set of K orbitals there will be $\binom{K}{N}$ Slater determinants. Minimizing $E[\Psi] = E(c_1, c_2, \dots)$ amounts then to a high-dimensional optimization problem. As $E(c_1, c_2, \dots)$ has no local minima, this can be done using a steepest descent method, e.g., the Lanczos method [11]. It involves the repeated application of the Hamiltonian to the trial function. When working with a basis set, a Hamiltonian (2) with pair interaction only couples Slater determinants that differ in at most two orbitals. Thus, the matrix representation of H in Slater-determinant space is reasonably sparse so that the matrix-vector product can be efficiently calculated. Nevertheless this method, called *configuration interaction (CI)* as it describes the interplay of Slater determinants (electron configurations), is limited to quite small systems by the sheer number of Slater determinants spanning the Hilbert space, or, equivalently, by the number of parameters c_{α} that need to be simultaneously optimized: For a system with 25 electrons and just 50 basis functions, the number of parameter is already above 10^{14} , i.e., requiring a peta byte of memory just for storing the parameters c_{α} . A way out might be to consider only ‘‘important’’ Slater determinants. It turns out that the variational energy converges, however, only slowly with the number of determinants included in the calculation. Moreover, when we want to study systems of increasing size a truncated CI easily leads to size-consistency problems [2].

An alternative to the full-CI ansatz are wave functions that capture the strongest effects of electron correlation with only a small number of parameters. To identify the major effect of electron correlation on the wave function, we return to the energy expectation value (30). Considered as a wave function functional, the stationarity condition

$$0 = \frac{\delta E}{\delta \Psi} = \frac{H|\Psi\rangle}{\langle \Psi | \Psi \rangle} - \frac{\langle \Psi | H | \Psi \rangle}{\langle \Psi | \Psi \rangle^2} |\Psi\rangle \quad (31)$$

is equivalent to the Schrödinger equation $H\Psi(\mathbf{r}) = E\Psi(\mathbf{r})$. Dividing by the wave function we obtain the *local energy*

$$E_{\text{loc}}(\mathbf{r}) = \frac{H\Psi(\mathbf{r})}{\Psi(\mathbf{r})}, \quad (32)$$

which is constant for eigenstates of H , i.e., its variance is zero (*zero variance property*). We can thus find eigenstates by minimizing the variance of the local energy (*variance minimization*)

$$\sigma^2[\Psi] = \int |E_{\text{loc}}(\mathbf{r})|^2 |\Psi(\mathbf{r})|^2 d\mathbf{r} - \left(\int E_{\text{loc}}(\mathbf{r}) |\Psi(\mathbf{r})|^2 d\mathbf{r} \right)^2 = \langle \Psi | H^2 | \Psi \rangle - \langle \Psi | H | \Psi \rangle^2. \quad (33)$$

This approach can also be employed for constructing good trial wave functions.

We might think that, as the solution of a second-order differential equation, wave functions are smooth with continuous first derivative. This is, however, not true at singularities in the potential. A well-known example is the hydrogen atom. Its ground state fulfills

$$H\varphi_{1s}(\vec{r}) = -\frac{1}{2} \vec{\nabla}^2 \varphi_{1s}(\vec{r}) - \frac{1}{r} \varphi_{1s}(\vec{r}) = E_{1s} \varphi_{1s}(\vec{r}). \quad (34)$$

For $r \rightarrow 0$, the potential energy diverges while $H\varphi_{1s}(\vec{r})$ remains finite. For this reason, the $1s$ function goes to a finite value at the position of the nucleus, producing a *cusp* \wedge , i.e., a discontinuity in the first derivative, which gives rise to the canceling divergence in the kinetic energy. The cancelation condition determining the cusp in the wave function, in the case of hydrogen $\varphi_{1s} \sim \exp(-\sqrt{x^2 + y^2 + z^2})$, is called the *cusp condition* [12]. Removing divergences in the local energy by implementing the cusp condition is the most important step towards reducing the variance of $E_{\text{loc}}(\mathbf{r})$, i.e., constructing good variational wave functions.

The cusps at the position of the nuclei are built into the single-particle orbitals obtained from a mean-field solution of (1). The many-body eigenstates will, however, also have cusps when two electrons meet ($\vec{r}_i \rightarrow \vec{r}_j$). These cusps are, of course, not easily reproduced by a linear combination of Slater determinants, which explains the slow convergence of CI expansions.

To derive the cusp conditions, we start with the electron-nucleus cusp. Following the example of hydrogen, we write the wave function close to a nucleus of charge Z as $\exp(-u_Z(r))$, where r is the distance of the electron from the nucleus. For r close to zero the local energy is

$$E_{\text{loc}}(r) = -\frac{1}{2} \frac{\left(\frac{d^2}{dr^2} + \frac{2}{r} \frac{d}{dr} \right) e^{-u_Z(r)}}{e^{-u_Z(r)}} - \frac{Z}{r} = -\frac{-u_Z''(r) + u_Z'(r)^2 - \frac{2u_Z'(r)}{r}}{2} - \frac{Z}{r}. \quad (35)$$

Thus, it stays finite for $r \rightarrow 0$ when

$$\left. \frac{du_Z}{dr} \right|_{r=0} = +Z. \quad (36)$$

For electrons, the cusp condition will depend on their relative spin orientation. Electrons with opposite spin need not be antisymmetrized so that we can write the wave function when the electrons are close to each other as $\exp(-u_{\sigma,-\sigma}(r))$ with $r = |\mathbf{r}_1 - \mathbf{r}_2|$. The situation is almost the same as for the electron-nucleon cusp, except that (i) electrons repel each other and (ii) we now have two electronic degrees of freedom, i.e., we get contributions from the kinetic energy operator for both electrons, resulting in

$$\left. \frac{du_{\sigma,-\sigma}}{dr} \right|_{r=0} = -\frac{1}{2}. \quad (37)$$

For electrons with parallel spin, the wave function must be antisymmetric in the electron coordinates, i.e., there must be a *nodal surface* separating the region where the wave function is positive from that where it is negative. For $\mathbf{r}_1 \approx \mathbf{r}_2$ we can approximate the nodal surface by $\mathbf{a} \cdot \mathbf{r} = 0$, which is a plane when we keep one of the electron coordinates fixed. We can then write the antisymmetric wave function close to $r = 0$ as $\mathbf{a} \cdot \mathbf{r} \exp(-u_{\sigma,\sigma}(r))$. Removing the singularity in the local energy now requires [4]

$$\left. \frac{du_{\sigma,\sigma}}{dr} \right|_{r=0} = -\frac{1}{4}. \quad (38)$$

Thus, the correlation cusp for opposite-spin electrons \sphericalangle affects the wave function more than that for parallel spins \sphericalhook since electrons with the same spin already tend to avoid each other as a consequence of exchange.

The cusp conditions just tell us the form of the wave function right at the singularity. To put this information into a usable wave function, we have to parametrize the electron-electron functions $u_{\sigma,\sigma'}(r)$ for finite r . This is typically done by writing $u(r)$ as a rational function that fulfills the cusp condition for $r \rightarrow 0$ and goes to a constant for $r \rightarrow \infty$. To ensure antisymmetry and the electron-nucleus cusps, the electron-electron correlators are multiplied onto a Slater determinant. This gives the *Jastrow wave function* [14]

$$\Psi_J(\mathbf{r}_1, \sigma_1; \dots; \mathbf{r}_N, \sigma_N) = \Phi(\mathbf{r}_1, \sigma_1; \dots; \mathbf{r}_N, \sigma_N) \prod_{i < j} e^{-u_{\sigma_i, \sigma_j}(r_{ij})}. \quad (39)$$

The product of pair functions is called the *Jastrow factor*. It will tend to reduce the amplitude of the Slater determinant when electrons come close to each other, i.e., it introduces a correlation hole. For systems with inhomogeneous charge density this means that the Jastrow factor pushes electrons away from regions of high charge-density, where the probability of two electrons approaching each other is largest. This can be compensated by introducing single-electron terms in the Jastrow factor [15]. That is particularly important when the Slater determinant used in (39) accurately describes the charge density of the system, e.g., from density-functional theory.

Having chosen parametrizations for $u_{\sigma,\sigma'}(r)$ and the single-electron term, the variational approach looks straightforward: just minimize the energy expectation value $\langle \Psi_J | H | \Psi_J \rangle / \langle \Psi_J | \Psi_J \rangle$ with respect to the (relatively few) Jastrow parameters. The pair functions, however, make it impossible to evaluate the expectation value other than by integrating over all electron configurations

$$\frac{\langle \Psi_J | H | \Psi_J \rangle}{\langle \Psi_J | \Psi_J \rangle} = \frac{\int d\mathbf{r}_1 \cdots d\mathbf{r}_N \overline{\Psi_J(\mathbf{r}_1, \sigma_1; \dots; \mathbf{r}_N, \sigma_N)} H \Psi_J(\mathbf{r}_1, \sigma_1; \dots; \mathbf{r}_N, \sigma_N)}{\int d\mathbf{r}_1 \cdots d\mathbf{r}_N |\Psi_J(\mathbf{r}_1, \sigma_1; \dots; \mathbf{r}_N, \sigma_N)|^2} \quad (40)$$

This $3N$ -dimensional integral is best done using stochastic sampling – variational Monte Carlo. What improvements in energy can we expect? Typically, optimizing a good trial function will lower the energy expectation value by only a few percent of the energy calculated with just the mean-field Slater determinant. This might seem little reward for the considerable effort. We

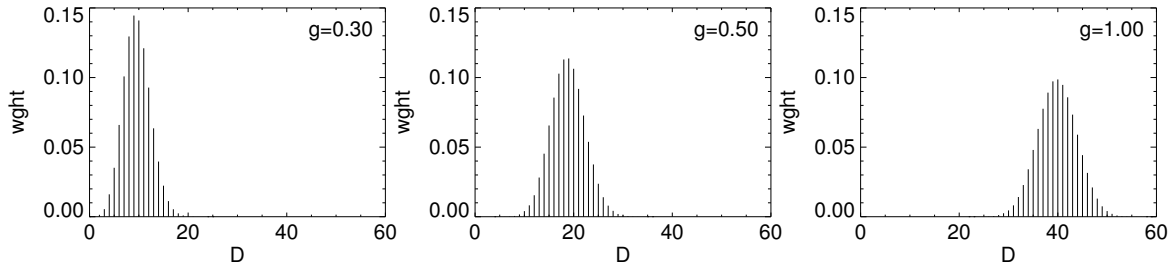


Fig. 3: Weight of configurations with given number D of double occupancies for Gutzwiller wave functions $\Psi_T(R) = g^{D(R)} \Phi(R)$. Reducing the Gutzwiller factor g suppresses configurations with high Coulomb energy $E_{\text{Coul}}(R) = U D(R)$ at the expense of increasing the kinetic energy. The results shown are for a Hubbard model on a square lattice of 16×16 sites with periodic boundary conditions and 101 electrons of each spin. For the uncorrelated Slater determinant ($g = 1$) the distribution is centered around $D = N_{\text{site}} n_{\uparrow} n_{\downarrow} = 16^2 (101/16^2)^2 \approx 40$.

have, however, to keep in mind that the effects of correlation, essentially the integral over the correlation-hole, are very small compared to the Coulomb energy of the uncorrelated charge density (Hartree energy) and the kinetic term. So correlation effects are barely noticeable on the scale of the total energy. The dominating role of the Hartree energy also becomes apparent when comparing the charge density of a solid to a simple superposition of atomic charge densities: the bonding induces barely noticeable changes, see, e.g., Fig. 1 in [16]. A more sensible benchmark than the change in total energy is how much of the *correlation energy*, i.e., the difference between the Hartree-Fock and the exact energy, is captured. On this count, variational wave functions fare much better: they typically recover roughly 90% of the correlation energy. Still, correlations are a subtle effect also on this energy scale, and variational methods are usually not sufficient for reaching chemical accuracy.

When working in second quantization with a finite (and therefore incomplete) basis set, we cannot describe two electrons coming arbitrarily close to each other. So there are no cusp conditions here. Still, we can correlate the electrons in the orbitals of the basis set by introducing correlation factors of the form $\exp(-\eta D)$, where D is a two-body operator. Such trial wave functions, with $D = \sum_i n_{i\uparrow} n_{i\downarrow}$ the number of doubly occupied sites, were introduced by Gutzwiller [17] as variational states for the Hubbard model

$$H = -t \sum_{ij,\sigma} c_{j\sigma}^\dagger c_{i\sigma} + U \sum_i n_{i\uparrow} n_{i\downarrow}. \quad (41)$$

The *Gutzwiller wave function* (GWF), with $|\Phi\rangle$ a mean-field solution of H , can be written as

$$|\Psi_T\rangle = e^{-\eta \sum_i n_{i\uparrow} n_{i\downarrow}} |\Phi\rangle = g^{\sum_i n_{i\uparrow} n_{i\downarrow}} |\Phi\rangle = \prod_i (1 - (1 - g) n_{i\uparrow} n_{i\downarrow}) |\Phi\rangle, \quad (42)$$

where $g = \exp(-\eta)$ and the final equality arises from the fact that $n_{i\uparrow} n_{i\downarrow}$ can only take the values 0 or 1. The role of the Gutzwiller parameter $g \in [0, 1]$ is to reduce the number of doubly occupied sites relative to the mean-field solution $|\Phi\rangle$, thus reducing the Coulomb repulsion at the expense of increasing the kinetic energy. This is illustrated in Fig. 3. Introducing more general two-body operators D , Gutzwiller wave functions can be devised for realistic multi-band models. See [18] for a nice introduction.

2.1 Variational Monte Carlo

As seen in (40), evaluating the energy expectation value for a Jastrow wave function involves the integration over the $3N$ -dimensional configuration space of the electrons. The key for doing this using stochastic sampling is again the local energy, which allows us to rewrite (40) as

$$\frac{\langle \Psi_J | H | \Psi_J \rangle}{\langle \Psi_J | \Psi_J \rangle} = \frac{\int d\mathbf{r}_1 \cdots d\mathbf{r}_N E_{\text{loc}}(\mathbf{r}_1, \sigma_1; \dots; \mathbf{r}_N, \sigma_N) |\Psi_J(\mathbf{r}_1, \sigma_1; \dots; \mathbf{r}_N, \sigma_N)|^2}{\int d\mathbf{r}_1 \cdots d\mathbf{r}_N |\Psi_J(\mathbf{r}_1, \sigma_1; \dots; \mathbf{r}_N, \sigma_N)|^2}. \quad (43)$$

As it is non-negative and normalized,

$$p(\mathbf{r}_1, \sigma_1; \dots; \mathbf{r}_N, \sigma_N) = \frac{|\Psi_J(\mathbf{r}_1, \sigma_1; \dots; \mathbf{r}_N, \sigma_N)|^2}{\int d\mathbf{r}_1 \cdots d\mathbf{r}_N |\Psi_J(\mathbf{r}_1, \sigma_1; \dots; \mathbf{r}_N, \sigma_N)|^2} \quad (44)$$

is a probability distribution function on the configuration space, so that we can evaluate (43) by sampling configurations $R = (\mathbf{r}_1, \sigma_1; \dots; \mathbf{r}_N, \sigma_N)$ with probability $p(R)$ and average the corresponding local energy $E_{\text{loc}}(R)$.

The same approach works for Hamiltonians written in second quantization, the main difference being that in this case the electron configurations are discrete, specifying the occupation of the orbitals used in second quantization. In the following, we specialize to the case of the simple Hubbard model (41) with one orbital per site. Denoting by R an electron configuration, specifying on which site the electrons are located as well as their spin, we can write the energy expectation value of a trial function Ψ_T as

$$E_T = \frac{\langle \Psi_T | H | \Psi_T \rangle}{\langle \Psi_T | \Psi_T \rangle} = \frac{\sum_R E_{\text{loc}}(R) \Psi_T^2(R)}{\sum_R \Psi_T^2(R)}, \quad (45)$$

with the local energy

$$E_{\text{loc}}(R) = \sum_{R'} \frac{\langle \Psi_T | R' \rangle \langle R' | H | R \rangle}{\langle \Psi_T | R \rangle} = \sum_{R' \neq R} t \frac{\Psi_T(R')}{\Psi_T(R)} + U D(R). \quad (46)$$

If the Hamiltonian allows only hopping to near neighbors, the sum over R' in the local energy scales with the number of near neighbors times the number of electrons in the system. In contrast, the sum over R in (45) is over *all* configurations, i.e., of the order of the dimension of the Hilbert space. With increasing system size this rapidly becomes extremely large. To give an impression, the dimension of the Hilbert space for the model shown in Fig. 3 is $\binom{16^2}{101} \times \binom{16^2}{101}$, which is larger than 10^{146} . So it seems quite impossible to do the sum in (45). Even generating configurations at a rate of 3.3 GHz, we could visit just 10^{17} configurations per year. It is the magic of stochastic methods that sums over such spaces can still be done to an astonishing accuracy.

The idea of *variational Monte Carlo* [19, 20] is to perform a random walk in the space of configurations, with transition probabilities $p(R \rightarrow R')$ chosen such that the configurations R_{VMC} in the random walk have the probability distribution function $\Psi_T^2(R)$. Then

$$E_{\text{VMC}} = \frac{\sum_{R_{\text{VMC}}} E_{\text{loc}}(R_{\text{VMC}})}{\sum_{R_{\text{VMC}}} 1} \approx \frac{\sum_R E_{\text{loc}}(R) \Psi_T^2(R)}{\sum_R \Psi_T^2(R)} = E_T. \quad (47)$$

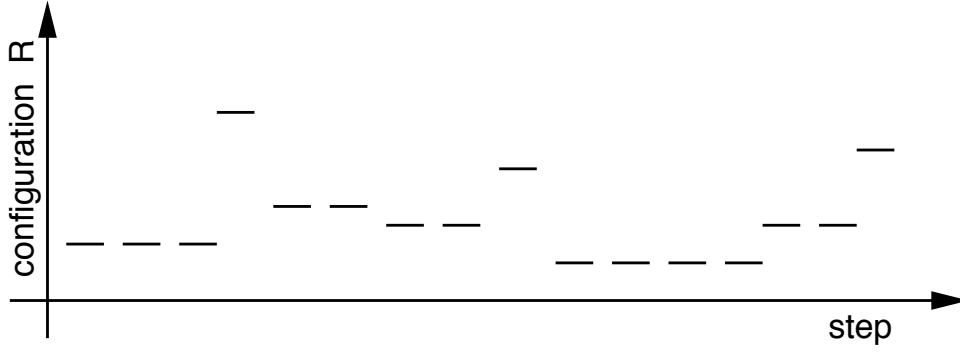


Fig. 4: Illustration of the random walk in configuration space.

The transition probabilities can be determined from detailed balance

$$\Psi_T^2(R) p(R \rightarrow R') = \Psi_T^2(R') p(R' \rightarrow R), \quad (48)$$

which gives $p(R \rightarrow R') = 1/N \min(1, \Psi_T^2(R')/\Psi_T^2(R))$, with N being the maximum number of possible transitions. It is sufficient to consider only transitions between configurations that are connected by the Hamiltonian, i.e., transitions in which one electron hops to a neighboring site. The standard prescription is then to propose a transition $R \rightarrow R'$ with probability $1/N$ and accept it with probability $\min(1, \Psi_T^2(R')/\Psi_T^2(R))$. This works well when U is not too large. For strongly correlated systems, however, the random walk will stay for long times in configurations with a small number of double occupancies $D(R)$, since most of the proposed moves will increase D and hence be rejected with probability $\approx 1 - g^{D(R')-D(R)}$.

Fortunately, there is a way to integrate-out the time the walk stays in a given configuration [21]. To see how, we first observe that for the local energy (46) the ratio of the wave functions for all transitions induced by the Hamiltonian have to be calculated. This in turn means that we also know all transition probabilities $p(R \rightarrow R')$. We can therefore eliminate any rejection, i.e., accept with probability one, by proposing moves $R \rightarrow R'$, ($R' \neq R$), with probabilities

$$\tilde{p}(R \rightarrow R') = \frac{p(R \rightarrow R')}{\sum_{R'} p(R \rightarrow R')} = \frac{p(R \rightarrow R')}{1 - p_{\text{stay}}(R)}. \quad (49)$$

Checking detailed balance (48) we find that now we are sampling configurations \tilde{R}_{VMC} from the probability distribution function $\Psi_T^2(R) (1 - p_{\text{stay}}(R))$. To compensate for this, we assign a weight $w(R) = 1/(1 - p_{\text{stay}}(R))$ to each configuration R . The energy expectation value is then given by

$$E_T \approx \frac{\sum_{\tilde{R}_{\text{VMC}}} w(\tilde{R}_{\text{VMC}}) E_{\text{loc}}(\tilde{R}_{\text{VMC}})}{\sum_{\tilde{R}_{\text{VMC}}} w(\tilde{R}_{\text{VMC}})}. \quad (50)$$

The above method is very efficient since it ensures that in every Monte Carlo step a new configuration is created. Instead of staying in a configuration where Ψ_T is large, this configuration is weighted with the expectation value of the number of steps the simple Metropolis algorithm would stay there. This is particularly convenient for simulations of systems with strong correlations: instead of having to do longer and longer runs as U is increased, the above method produces, for a fixed number of Monte Carlo steps, results with comparable error estimates.

2.2 Correlated sampling

The essence of the variational method is the minimization of the energy expectation value (45) as a function of the variational parameters in the trial function. To this end, we could simply perform independent VMC calculations for a set of different parameters. It is, however, difficult to compare the energies from independent calculations since each VMC result comes with its own statistical errors. This problem can be avoided with *correlated sampling* [19, 22]. The idea is to use the same random walk in calculating the expectation value for different trial functions. This reduces the relative errors and hence makes it easier to find the minimum.

Let us assume that we have generated a random walk $\{R_{\text{VMC}}\}$ for the trial function Ψ_T . Using the *same* random walk, we can also estimate the energy expectation value (47) for a different trial function $\tilde{\Psi}_T$. To do so we have to compensate for the fact that the configurations have the probability distribution Ψ_T^2 instead of $\tilde{\Psi}_T^2$ by introducing reweighting factors

$$\tilde{E}_T \approx \frac{\sum_{R_{\text{VMC}}} \tilde{E}_{\text{loc}}(R) \tilde{\Psi}_T^2(R)/\Psi_T^2(R)}{\sum_{R_{\text{VMC}}} \tilde{\Psi}_T^2(R)/\Psi_T^2(R)}. \quad (51)$$

Likewise, (50) is reweighted into

$$\tilde{E}_T \approx \frac{\sum_{\bar{R}_{\text{VMC}}} w(\bar{R}) \tilde{E}_{\text{loc}}(\bar{R}) \tilde{\Psi}_T^2(\bar{R})/\Psi_T^2(\bar{R})}{\sum_{\bar{R}_{\text{VMC}}} w(\bar{R}) \tilde{\Psi}_T^2(\bar{R})/\Psi_T^2(\bar{R})}. \quad (52)$$

Also, the local energy $\tilde{E}_{\text{loc}}(R)$ can be rewritten such that the new trial function appears only in ratios with the old one. For Gutzwiller functions this implies a drastic simplification. Since they differ only in the Gutzwiller factor, the Slater determinants cancel, leaving only powers $(\tilde{g}/g)^{D(R)}$

$$E_T(\tilde{g}) \approx \frac{\sum_{R_{\text{VMC}}} \tilde{E}_{\text{loc}}(R) (\tilde{g}/g)^{2D(R)}}{\sum_{R_{\text{VMC}}} (\tilde{g}/g)^{2D(R)}} \quad (53)$$

and

$$\tilde{E}_{\text{loc}}(R) = -t \sum_{R' \neq R} (\tilde{g}/g)^{D(R')-D(R)} \frac{\Psi_T(R')}{\Psi_T(R)} + U D(R). \quad (54)$$

As the number of doubly occupied sites $D(R)$ for a configuration R is an *integer*, we can rearrange the sums in (53) and (54) into polynomials in \tilde{g}/g . The energy expectation value for any Gutzwiller parameter \tilde{g} is then given by a rational function in the variable \tilde{g}/g , where the coefficients only depend on the fixed trial function $|\Psi(g)\rangle$.

It is then clear how we proceed to optimize the Gutzwiller parameter in variational Monte Carlo [21]: we first pick a reasonable g and perform a VMC run for $|\Psi(g)\rangle$ during which we also estimate the coefficients of the above polynomials. We can then easily calculate $E_T(\tilde{g})$ by evaluating the rational function in \tilde{g}/g . Since the number of non-vanishing coefficients typically is only of the order of a few tens (see the distribution of weights shown in Figure 3), this is a very efficient process.

Figure 5 shows how the method works in practice. Although we deliberately picked a bad starting point, we still find the correct minimum. Of course, this will not be true for the whole

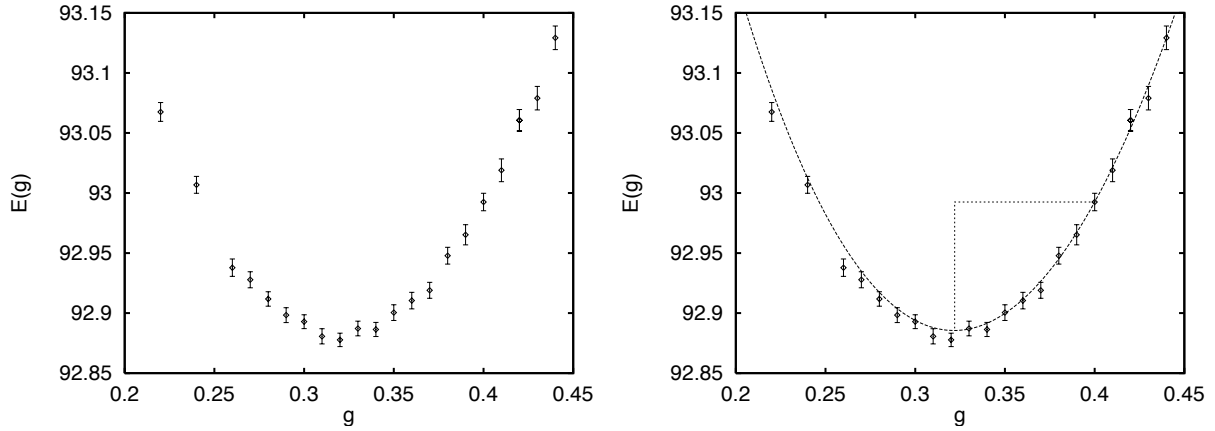


Fig. 5: *Optimizing the Gutzwiller parameter g : The left-hand panel shows the straightforward approach of calculating the variational energy for a number of different values of g in separate VMC runs. The curve in the right-hand panel shows the result of a single correlated sampling run, calculated at $g = 0.4$. The predicted minimum is indicated by the dotted line and corresponds to the actual minimum. The calculations are for a cluster of 32 C_{60} molecules with 48+48 electrons (half-filling) and $U = 1.0$ eV [23].*

range of Gutzwiller parameters. When \tilde{g} differs too much from g , the method breaks down. To understand this we again turn to Figure 3. We see that most configurations in a random walk generated with, say, $g = 0.50$ will have about 20 doubly occupied sites. In the Monte Carlo run we therefore sample the coefficients for $(\tilde{g}/g)^{2 \times 20}$ best, while the statistics for much larger or smaller powers is poor. But it is exactly these poorly sampled coefficients that we need for calculating the energy expectation value of trial functions with \tilde{g} much different from g . We can thus use the overlap of the wave functions $\langle \Psi(\tilde{g}) | \Psi(g) \rangle$ as a measure of the reliability of the calculated energy $E_T(\tilde{g})$. Like the energy expectation value itself, it can be recast in the form of polynomials, the coefficients of which can be sampled during the VMC run

$$\langle \Psi(\tilde{g}) | \Psi(g) \rangle = \frac{\sum_R \tilde{\Psi}(R) \Psi(R)}{\sqrt{\sum_R \tilde{\Psi}^2(R) \sum_R \Psi^2(R)}} = \frac{\sum_{R_{\text{VMC}}} (\tilde{g}/g)^{D(R)}}{\sqrt{\sum_{R_{\text{VMC}}} (\tilde{g}/g)^{2D(R)} \sum_{R_{\text{VMC}}} 1}}. \quad (55)$$

Figure 6 shows how the reliability of correlated sampling results depends on the overlap of with the trial function that is used in the VMC run.

There are some straightforward modifications of the scheme we have described above. Often, it is more appropriate to minimize the variance in the local energy $\sigma^2(g)$ rather than the energy $E(g)$ [22]. Since the variance can also be rewritten in terms of a rational function in \tilde{g}/g , variance minimization can be implemented in much the same way as the energy minimization that we have described here. Furthermore, it is clear that the method is not restricted to the plain Gutzwiller wave function but can be generalized to trial functions with more correlation factors of the type $r^{c(R)}$. As long as the correlation function $c(R)$ is integer-valued on the space of configurations, expectation values for such trial functions can still be rewritten as rational functions. The only difference to the simpler case described above is that now the rational function is multivariate, reflecting the fact that there is more than one variational parameter.

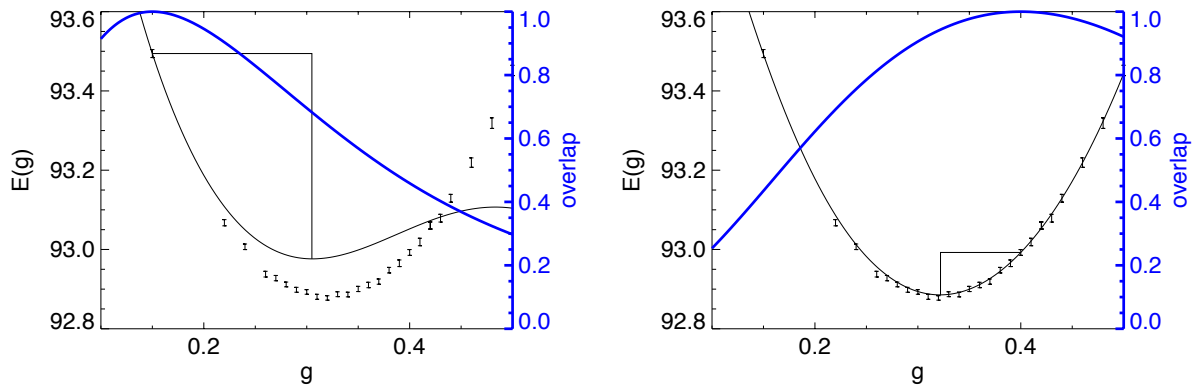


Fig. 6: The reliability of a correlated sampling run depends on the overlap of the trial function with the wave function at the predicted minimum. Left: inefficient sampling for small overlap. Right: reliable sampling for sufficiently large overlap. The thin line gives the energy curve obtained from the correlated sampling run, the thick line shows the overlap. The calculations are for the same system as in Figure 5.

2.3 Gutzwiller approximation

In Fig. 3 we found that we can estimate the number of doubly occupied sites in a non-interacting Slater determinant by simply assuming that the electrons of different spins are distributed uniformly over the lattice: $D \approx N_{\text{site}} n_{\uparrow} n_{\downarrow}$. In terms of electron configurations, this can be rephrased: all electron configurations R have the same weight in $|\Phi\rangle$, i.e., $|\Phi\rangle = \sum_R c_R |R\rangle$ with $|c_R|^2 = \text{const}$. This is the basic assumption of the Gutzwiller approximation (GA) [17, 24]. It provides surprisingly reliable estimates of the properties of the Gutzwiller wave function using simple combinatorics.

As electron correlation in the Hubbard model arises from the doubly occupied sites, it is reasonable to use the number of doubly occupied sites to characterize an electron configuration R . More specifically, we introduce the notation

- M : number of lattice sites ($= N_{\text{site}}$)
- N_{σ} : number of electrons with spin σ
- E : number of empty sites
- L_{σ} : number of sites with a single electron of spin σ
- D : number of doubly occupied sites

While the number of lattice sites and electrons is fixed for a given system, the other quantities have to fulfill physical constraints. A site is either empty, singly, or doubly occupied, i.e., $M = E + L_{\uparrow} + L_{\downarrow} + D$, and the electrons are on singly or doubly occupied sites, i.e., $N_{\sigma} = L_{\sigma} + D$. Given this notation, the number of configurations with a given D is obtained by distributing the empty, singly, and double occupied sites over the lattice

$$G(D) = \binom{M}{E} \binom{M-E}{L_{\uparrow}} \binom{M-E-L_{\uparrow}}{L_{\downarrow}} \binom{M-E-L_{\uparrow}-L_{\downarrow}}{D} = \frac{M!}{E!L_{\uparrow}!L_{\downarrow}!D!}. \quad (56)$$

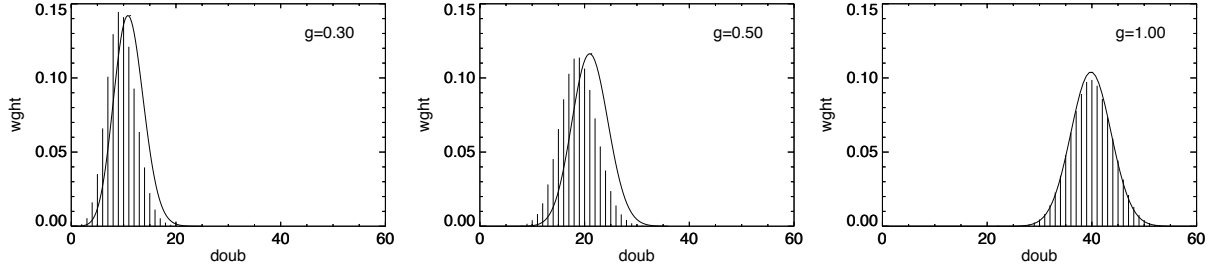


Fig. 7: Comparison of the weight of doubly occupied configurations for Gutzwiller wave functions (histograms) and as calculated in the Gutzwiller approximation (curves). The system is the same as in Figure 3.

Figure 7 shows that the distribution (56) matches that calculated for an uncorrelated Slater determinant almost perfectly. For a Gutzwiller wave function, the Gutzwiller parameter changes the GA-weights to $\sum_{R \text{ with } D \text{ double occs}} |c_R|^2 \propto G(D) g^{2D}$. Even for quite large correlation, i.e., small g , the agreement with the actual weights is surprisingly good. As we are dealing with quite large factorials, we can use Stirling's approximation $N! \sim \sqrt{2\pi N} \exp(N \ln(N) - N)$ to simplify (56)

$$\frac{G(D)}{G_{\text{tot}}} g^{2D} = \sqrt{\frac{n_{\uparrow}(1-n_{\uparrow})n_{\downarrow}(1-n_{\downarrow})}{2\pi M e l_{\uparrow} l_{\downarrow} d}} \left(\frac{n_{\uparrow}^{n_{\uparrow}}(1-n_{\uparrow})^{1-n_{\uparrow}} n_{\downarrow}^{n_{\downarrow}}(1-n_{\downarrow})^{1-n_{\downarrow}}}{e^e l_{\uparrow}^{l_{\uparrow}} l_{\downarrow}^{l_{\downarrow}} d^d} \right)^M \quad (57)$$

where $n_{\sigma} = N_{\sigma}/M$ and $d = D/M$, etc. From this we see that the distribution of double occupancies, as a function of d , narrows with increasing M . Thus, for general $g \in [0, 1]$, the density of double occupancies in the thermodynamic limit is given by the position of the maximum of the distribution. Using the asymptotics of the derivative of the gamma function $\Gamma(z)' = \Gamma(z)\Psi_0(z) \sim \Gamma(z) \ln(z)$, we find $g^2 = e d / (l_{\uparrow} l_{\downarrow})$, or, explicitly,

$$d(n_{\uparrow}, n_{\downarrow}; g) = -\frac{1}{2} \left(\frac{1}{1-g^2} - n_{\uparrow} - n_{\downarrow} \right) + \sqrt{\frac{1}{4} \left(\frac{1}{1-g^2} - n_{\uparrow} - n_{\downarrow} \right)^2 + \frac{n_{\uparrow} n_{\downarrow} g^2}{1-g^2}}, \quad (58)$$

i.e., in the thermodynamic limit the Gutzwiller parameter determines d . In the uncorrelated case it gives the familiar $d(g=1) = n_{\uparrow} n_{\downarrow}$ from Fig. 3, while in the opposite limit there are only double occupancies above half-filling: $d(g=0) = \max(0, n-1)$.

Similarly, we can estimate the overlap of wave functions with different Gutzwiller parameters, which is a measure of the efficiency of correlated sampling,

$$\langle \Psi(\tilde{g}) | \Psi(g) \rangle \sim \sum_D \frac{M!}{E! L_{\uparrow}! L_{\downarrow}! D!} (g\tilde{g})^D. \quad (59)$$

Expanding around $\tilde{g} = g$ we find that the overlap looks like a Gaussian: $\exp[-M(\tilde{g} - g)^2 / \sigma_0^2]$, with M the number of lattice sites. As expected, for fixed $\tilde{g} \neq g$, the overlap goes to zero exponentially with system size (orthogonality catastrophe). σ_0 is a function of g and the filling and generally decreases with g . This can be seen in Figure 7: for small g the weights are peaked more sharply than for larger Gutzwiller parameters. For half-filling, $\sigma_0 = \sqrt{2g} / 2(1+g)$. The relation between the overlap and the reliability of correlated sampling (53) is illustrated in Figure 6.

For the energy expectation value

$$E(g) = \frac{\langle \Psi(g) | H | \Psi(g) \rangle}{\langle \Psi(g) | \Psi(g) \rangle} = -2t \sum_{ij,\sigma} \frac{\langle \Psi(g) | c_{j\sigma}^\dagger c_{i\sigma} | \Psi(g) \rangle}{\langle \Psi(g) | \Psi(g) \rangle} + U D(g) \quad (60)$$

in the Gutzwiller approximation, the Hubbard energy is explicitly given through the relation (58) between g and the density of doubly occupied sites. For estimating the kinetic energy, we first observe that $\langle \Psi(g) | c_{j\sigma}^\dagger c_{i\sigma} | \Psi(g) \rangle / \langle \Psi(g) | \Psi(g) \rangle$ is the probability for an electron of spin σ to hop from site i to site j . The probability for a hop being allowed by the Pauli principle is $n_\sigma (1 - n_\sigma)$. In the Gutzwiller approximation there are more severe constraints on the hopping processes coming from the condition that the density of doubly occupied sites is fixed at (58). Thus, only hops from a singly occupied to an empty site (probability $l_\sigma e$) or from a doubly to a singly occupied site (probability $d l_{-\sigma}$) are allowed. Thus, replacing the Pauli constraint with the more severe Gutzwiller constraints reduces the hopping matrix elements of the uncorrelated Slater determinant by the *hopping reduction factor*

$$\gamma_\sigma(n_\sigma, g) = \frac{\left(\sqrt{l_\sigma e} + \sqrt{d l_{-\sigma}} \right)^2}{n_\sigma (1 - n_\sigma)}, \quad (61)$$

where we have added the amplitudes for the two allowed hopping processes. Using again the basic assumption of the Gutzwiller approximation that all configurations contribute the same, we find for the energy per site

$$\varepsilon_{\text{GA}}(g) = \sum_{\sigma} \gamma_\sigma(n_\sigma, g) \varepsilon_\sigma^{(0)}(n_\sigma) + U d(n_\uparrow, n_\downarrow; g), \quad (62)$$

where $\varepsilon_\sigma^{(0)}(n_\sigma)$ is the kinetic energy for the Slater determinant of the Gutzwiller wave functions. Optimizing the Gutzwiller parameter g thus means finding the best trade-off between lowering the Hubbard energy by reducing the density of double occupancies and the simultaneous increase in the (negative) kinetic energy due to the band narrowing proportional to the hopping reduction γ_σ . Because of the relation (58) between g and d we actually need not consider g but can minimize the energy using d as the parameter.

2.4 Brinkman-Rice transition

At half-filling ($n_\sigma = 1/2$) the expressions from the Gutzwiller approximation simplify significantly. The hopping reduction factor becomes $\gamma = 16d(1/2 - d)$, so we can write the energy expectation value per site as

$$\varepsilon(d) = 16 d (1/2 - d) \varepsilon^{(0)} + U d, \quad (63)$$

where $\varepsilon^{(0)}$ is the kinetic energy density of the uncorrelated system (both spins). Minimizing gives

$$d_{\text{min}}(U) = \frac{1}{4} + \frac{U}{32\varepsilon^{(0)}}. \quad (64)$$

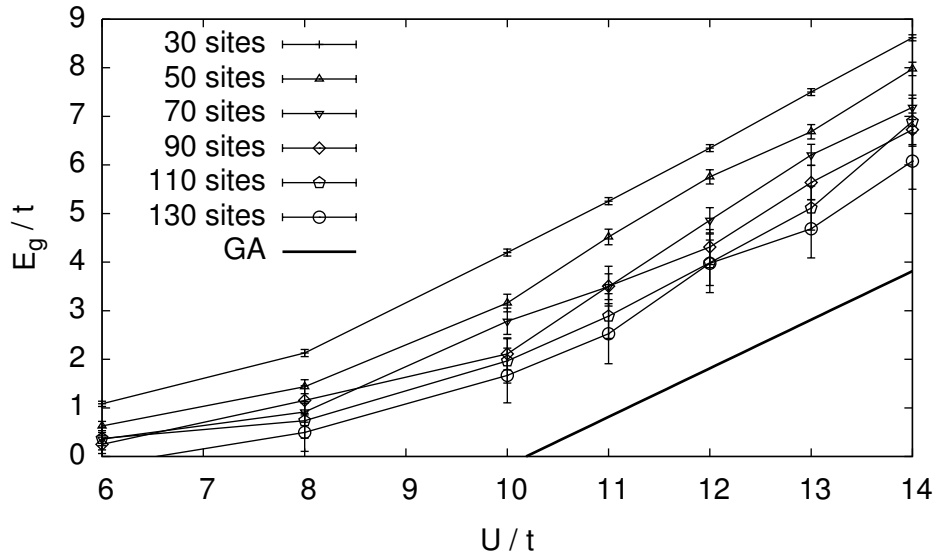


Fig. 8: Gap calculated by variational Monte Carlo for the Gutzwiller wave function on the finite one-dimensional Hubbard model with periodic boundary conditions (Hubbard rings). For 30-site rings a gap appears to open at $U \approx 6$. For larger rings the gap opens at slightly increasing values of U , and it looks as if the result of the Gutzwiller approximation is reached for large enough systems. But actually the opening of a gap is a pure finite-size effect, as a Gutzwiller wave function with metallic Slater determinant is always metallic, unless $g = 0$.

For the uncorrelated system this gives the familiar $d_{\min}(U = 0) = n_{\uparrow}n_{\downarrow}$. With increasing U , double occupancies are reduced until they vanish entirely at $U_c = 8|\varepsilon^{(0)}|$. From that point on, the system has no doubly occupied sites; the hopping reduction becomes $\gamma = 0$ suppressing all hopping, i.e., making the system an insulator. This is the Brinkman-Rice scenario for a half-filled band turning insulating [25].

We might wonder if we could see the metal-insulator transition in VMC calculations. The insulating state can be determined by calculating the gap

$$E_g(M) = E(N + 1) - 2E(N) + E(N - 1) \quad (65)$$

$$= \frac{\varepsilon(n + 1/M) - \varepsilon(n)}{1/M} - \frac{\varepsilon(n) - \varepsilon(n - 1/M)}{1/M} \quad (66)$$

$$\rightarrow \left. \frac{dE(n)}{dn} \right|_{n^+} - \left. \frac{dE(n)}{dn} \right|_{n^-} = \mu^+ - \mu^- . \quad (67)$$

Opening of the gap $E_g > 0$ indicates a jump in the chemical potential, i.e., an insulator. For an insulating half-filled system $N = M$ at large U we would expect $E_g \sim U$, since the system cannot avoid double occupancy with $M + 1$ electrons. Results for a simple Hubbard chain are shown in Figure 8. It appears that around $U_c = 32t/\pi \approx 10t$, the value predicted by the Gutzwiller approximation for the one-dimensional Hubbard model, the gap indeed starts to open proportionally to U . As the size of the Hubbard chain used in the simulation increases, the gap is slightly reduced, seemingly approaching the value predicted by the Gutzwiller approximation. This is, however, a pure finite-size effect.

For the one-dimensional Hubbard model, the ground state properties were actually calculated analytically by Metzner and Vollhardt [26]. For any finite U , the ground state energy $\varepsilon_{GWF}(n)$

has a continuous derivative at half-filling. So the Gutzwiller wave function always describes a metal, except for $g = 0$. This example should serve as a warning that finite-size extrapolations can be quite tricky. Here, even though the energy per site converges quickly to the exact result, having to take finite differences instead of derivatives in the evaluation of the gap for finite systems can create the appearance of a gapped system.

There is an elegant argument using the response of the energy to twisted boundary conditions that shows that, quite generally, Gutzwiller-type wave functions with a metallic Slater determinant are always metallic [27]. Consider a variational wave function

$$|\Psi\rangle = \prod_{\alpha} g_{\alpha}^{C_{\alpha}} |\Phi\rangle, \quad (68)$$

where $|\Phi\rangle$ is a Slater determinant and C_{α} a set of correlation functions (the simple Gutzwiller function uses only one correlation function, $\sum_i n_{i\uparrow} n_{i\downarrow}$). For twisted boundary conditions in direction \mathbf{c} on a finite simulation cell, moving an electron by the cell vector $\mathbf{c} = \mathbf{A}\mathbf{n}$ introduces a phase $\exp(i\mathbf{k} \cdot \mathbf{c})$. This phase can be absorbed into the Hamiltonian by transforming the creation/annihilation operators at site $\mathbf{A}\mathbf{j}$ into $c_{j\sigma} \rightarrow e^{i\mathbf{k} \cdot \mathbf{A}\mathbf{j}} c_{j\sigma}$ and introducing periodic boundary conditions. The Hamiltonian thus becomes dependent on \mathbf{k} with the hopping terms picking up a phase from the twisted boundary conditions, while in the Hubbard interaction the phases cancel

$$H(\mathbf{k}) = -t \sum_{ij,\sigma} e^{i\mathbf{k} \cdot \mathbf{A}(i-j)} c_{j\sigma}^{\dagger} c_{i\sigma} + U \sum_i n_{i\uparrow} n_{i\downarrow}. \quad (69)$$

The energy expectation value for the Gutzwiller wave function depends on k and the g_{α} , where the Gutzwiller parameters change with the boundary conditions as

$$E_G(k + dk, \{g_{\alpha}(k + dk)\}) = E_G(k, \{g_{\alpha}(k)\}) + \left(\frac{\partial E_G}{\partial k} + \sum_{\alpha} \frac{\partial E_G}{\partial g_{\alpha}} \frac{dg_{\alpha}}{dk} \right) dk + \mathcal{O}(dk^2). \quad (70)$$

The Gutzwiller parameters minimize E_G , i.e., the variations of the energy expectation value with respect to the g_{α} vanish. Solving the resulting linear system for the first-order term gives the dependence of the Gutzwiller parameters on the boundary conditions

$$\frac{dg_{\alpha}}{dk} = - \sum_{\beta} \left(\frac{\partial^2 E_G}{\partial g_{\beta} \partial g_{\alpha}} \right)^{-1} \left(\frac{\partial^2 E_G}{\partial g_{\beta} \partial k} \right), \quad (71)$$

while the second derivative of the energy with respect to the boundary conditions is

$$\frac{d^2 E_G}{dk^2} = \frac{d}{dk} \left(\frac{\partial E_G}{\partial k} + \sum_{\alpha} \frac{\partial E_G}{\partial g_{\alpha}} \frac{dg_{\alpha}}{dk} \right) = \frac{\partial^2 E_G}{\partial k^2} + \sum_{\alpha} \frac{\partial^2 E_G}{\partial k \partial g_{\alpha}} \frac{dg_{\alpha}}{dk}. \quad (72)$$

When the Gutzwiller factors in (68) are independent of the boundary conditions, e.g., the C_i are density or spin correlation functions, the explicit dependence of E_G on the boundary conditions k is only through the kinetic energy T . For a metallic Slater determinant the first term will then produce a non-vanishing conductivity for any U , except in the atomic limit $U \rightarrow \infty$.

The Brinkman-Rice transition is thus produced by the Gutzwiller approximation, although it is not present in the underlying Gutzwiller wave function, except in the limit $d \rightarrow \infty$, where the Gutzwiller approximation becomes exact [26].

3 Projection techniques

We can systematically improve on the variational results by using projection techniques [28]. The basic idea is surprisingly simple: when we operate with $\exp(-\tau H)$ on a wave function $|\Psi_T\rangle$ then, for large τ , the ground state $|\psi_0\rangle$ will dominate in the projected function, provided that the initial function had non-zero overlap with it. For a finite-dimensional Hamiltonian, where the spectrum is bounded not only from below but also from above, this imaginary-time propagation can be simplified to a matrix vector product

$$|\Psi^{(n+1)}\rangle = [1 - \tau(H - \bar{E}^{(n)})] |\Psi^{(n)}\rangle ; \quad |\Psi^{(0)}\rangle = |\Psi_T\rangle, \quad (73)$$

where τ has to be small enough and $\bar{E}^{(n)}$ is chosen to ensure normalization of the projected functions. To see under what conditions this converges to the ground state, we expand the starting function $|\Psi_T\rangle = \sum_i c_i |\Psi_i\rangle$ in eigenstates $H|\Psi_i\rangle = E_i|\Psi_i\rangle$. Then

$$|\Psi^{(n)}\rangle = \sum c_i \prod_n [1 - \tau(E_i - \bar{E}^{(n)})] |\Psi_i\rangle. \quad (74)$$

Convergence to $|\Psi_0\rangle$, up to normalization, is ensured if $c_i \neq 0$ and

$$|1 - \tau(E_0 - \bar{E}^{(n)})| > |1 - \tau(E_i - \bar{E}^{(n)})| \quad \forall i \neq 0. \quad (75)$$

For $\tau > 0$ we distinguish two cases

- $1 - \tau(E_0 - \bar{E}^{(n)}) > 1 - \tau(E_i - \bar{E}^{(n)})$, which leads to the trivial $E_0 < E_i$, and
- $1 - \tau(E_0 - \bar{E}^{(n)}) > -[1 - \tau(E_i - \bar{E}^{(n)})]$, from which follows that $2 > \tau(E_i + E_0 - 2\bar{E}^{(n)})$.

Thus, to secure convergence, one has to choose

$$0 < \tau < \frac{2}{E_{\max} + E_0 - 2\bar{E}^{(n)}} \quad (76)$$

which implies that $\bar{E}^{(n)} \in [E_0, E_{\max}]$ must lie inside the spectrum of H . In fact, for large n it will approach the ground state energy.

Because of the prohibitively large dimension of the many-body Hilbert space, the matrix vector product in (73) cannot be done exactly. Instead, we rewrite the equation in configuration space

$$\sum_{R'} |R'\rangle \langle R' | \Psi^{(n+1)} \rangle = \sum_{R, R'} |R'\rangle \underbrace{\langle R' | 1 - \tau(H - E_0) | R \rangle}_{=: F(R', R)} \langle R | \Psi^{(n)} \rangle \quad (77)$$

and perform the propagation in a stochastic sense: $|\Psi^{(n)}\rangle$ is represented by an ensemble of configurations R with weights $w(R)$. The transition matrix element $F(R', R)$ is rewritten as a transition probability $p(R \rightarrow R')$ times a normalization factor $m(R', R)$. The iteration (77) is then stochastically performed as follows: for each R we pick, out of the set of all allowed configurations, *one* new configuration R' with probability $p(R \rightarrow R')$ and multiply its weight by $m(R', R)$. Then the new ensemble of configurations R' with their respective weights represents the new function $|\Psi^{(n+1)}\rangle$.

3.1 Importance sampling

Importance sampling introduces a guiding function $|\Psi_G\rangle$ to decisively improve the efficiency of the stochastic projection by enhancing transitions from configurations where the trial function is small to configurations with large trial function, i.e., by replacing the transition matrix element $F(R', R)$ with $G(R', R) = \langle R' | \Psi_G \rangle F(R', R) / \langle R | \Psi_G \rangle$. The propagation is then given by

$$\sum_{R'} |R'\rangle \langle R' | \Psi_G \rangle \langle R' | \Psi^{(n+1)} \rangle = \sum_{R, R'} |R'\rangle G(R', R) \langle R | \Psi_G \rangle \langle R | \Psi^{(n)} \rangle \quad (78)$$

and the ensemble of configurations now represents the product $\Psi_G \Psi^{(n)}$. This means that the probability distribution function $P^{(n)}(w, R) dw$ of configurations R with weight w is such that

$$\Psi_G(R) \Psi^{(n)}(R) = \int w P^{(n)}(w, R) dw. \quad (79)$$

To see this, we rewrite the matrix element of the propagation as

$$G(R', R) = p(R \rightarrow R') m(R', R), \quad (80)$$

where $p(R \rightarrow R')$ is the probability for the random walk to move from configuration R to R' and the weight $m(R', R)$ takes care of the normalization. For the probability distribution function this implies

$$P^{(n+1)}(w', R') dw' = \sum_R p(R \rightarrow R') P^{(n)}\left(\frac{w'}{m(R', R)}, R\right) \frac{dw'}{m(R', R)} \quad (81)$$

and hence

$$\begin{aligned} \int w' P^{(n+1)}(w', R') dw' &= \sum_R p(R \rightarrow R') \int w' P^{(n)}\left(\frac{w'}{m(R', R)}, R\right) \frac{dw'}{m(R', R)} \\ &= \sum_R p(R \rightarrow R') m(R', R) \int w P^{(n)}(w, R) dw \\ &= \sum_R G(R', R) \Psi_G(R) \Psi^{(n)}(R) \\ &= \Psi_G(R') \Psi^{(n+1)}(R'). \end{aligned}$$

After a large number n of iterations, the ground-state energy is given by the *mixed estimator*

$$E_0^{(n)} = \frac{\langle \Psi_G | H | \Psi^{(n)} \rangle}{\langle \Psi_G | \Psi^{(n)} \rangle} \approx \frac{\sum_R E_{\text{loc}}(R) w^{(n)}(R)}{\sum_R w^{(n)}(R)}. \quad (82)$$

When we start the iteration from the guiding function, we can generate the configurations for the initial state $\Psi_G(R) \Psi^{(0)}(R)$ by a variational Monte Carlo run for Ψ_G . For this practical reason one usually chooses the guiding function to be the VMC trial function. In the following we therefore use Ψ_G and Ψ_T synonymously.

Hamiltonian	Hilbert space		
	full	restricted	system
H	-1.2238	-1.2203	4×4 -Hubbard model, 5 + 5 electrons
H_{eff}	-1.2236	-1.2201	$U = 4t$, free electron nodes
H	8.46487	8.46490	4 C_{60} molecules, 5 + 6 electrons
H_{eff}	8.46557	8.46728	$U = 1.0$ eV, $U_0 = 0.1$ eV
H	10.69937	10.69937	4 C_{60} molecules, 6 + 6 electrons
H_{eff}	10.70045	10.70045	$U = 1.0$ eV, $U_0 = 0.1$ eV
H	19.50941	19.54933	4 C_{60} molecules, 7 + 8 electrons
H_{eff}	19.51073	19.55372	$U = 1.0$ eV, $U_0 = 0$ eV
H	19.50941	19.50941	4 C_{60} molecules, 7 + 8 electrons
H_{eff}	19.50941	19.51068	$U = 1.0$ eV, $U_0 = 0.1$ eV

Table 1: Approximations in FNMC: results of exact diagonalization of the true/effective Hamiltonian on the full/restricted Hilbert space for the Hubbard model and a model of solid K_3C_{60} [23]. For the meaning of U_0 see section 3.3.2.

3.2 Fixed-node Monte Carlo

As long as the evolution operator has only non-negative matrix elements $G(R', R)$, all weights $w(R)$ will be positive. If, however, G has negative matrix elements there will be configurations with negative as well as positive weight. Their contributions to the estimator (82) tend to cancel so that eventually the statistical error dominates, rendering the simulation useless. This is the infamous *sign problem*. A straightforward way to get rid of the sign problem is to remove the offending matrix elements from the Hamiltonian, thus defining a new Hamiltonian H_{eff} by

$$\langle R' | H_{\text{eff}} | R \rangle = \begin{cases} 0 & \text{if } G(R', R) < 0 \\ \langle R' | H | R \rangle & \text{else} \end{cases} \quad (83)$$

for $R' \neq R$. For each off-diagonal element $\langle R' | H | R \rangle$ that has been removed, a term is added to the diagonal

$$\langle R | H_{\text{eff}} | R \rangle = \langle R | H | R \rangle + \sum_{R'} \Psi_G(R') \langle R' | H | R \rangle / \Psi_G(R). \quad (84)$$

This is the *fixed-node approximation* for lattice Hamiltonians [29]. By construction, H_{eff} is free of the sign-problem, and it gives a variational energy, i.e. $E_0^{\text{eff}} \geq E_0$. The exact ground-state energy is obtained if $\Psi_G(R') / \Psi_G(R) = \Psi_0(R') / \Psi_0(R)$ for all R, R' with $G(R', R) < 0$.

It is important to realize that fixed-node Monte Carlo involves two distinct approximations. The obvious approximation is replacing the true Hamiltonian by the effective Hamiltonian H_{eff} . Somewhat less obvious is the fact that importance sampling amounts to restricting the accessible region of the Hilbert space to configurations where $\Psi_G(R) \neq 0$. For small systems these two approximations can be considered separately by performing exact diagonalization for the effective Hamiltonian on the full Hilbert space and by diagonalizing the true Hamiltonian on the restricted Hilbert space. Finally, the fixed-node Monte Carlo energy can be determined by diagonalizing H_{eff} on the restricted Hilbert space. Examples are given in Table 1.

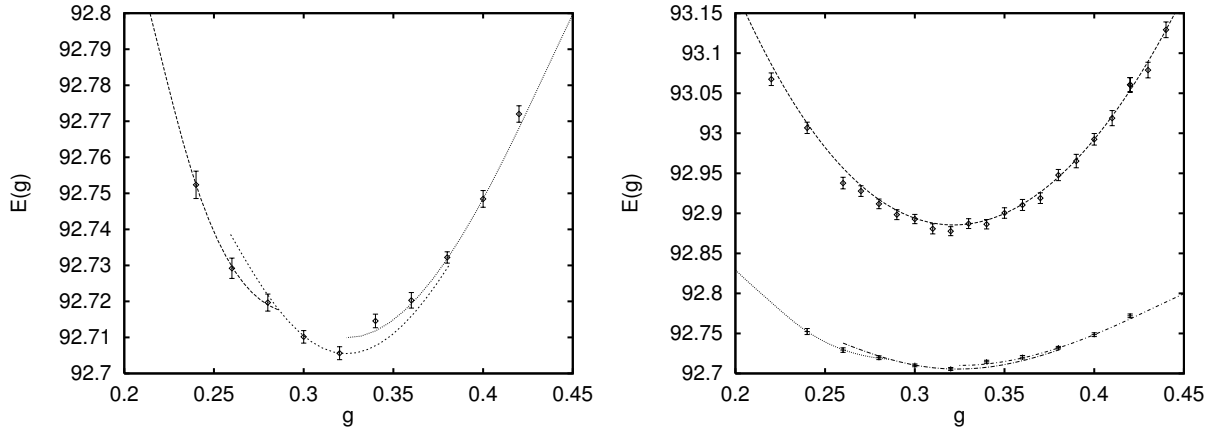


Fig. 9: Optimizing the Gutzwiller parameter g in fixed-node Monte Carlo: the left-hand panel shows how the correlated sampling approach for the Gutzwiller parameter g works for FNMC. The error bars give the results of independent Monte Carlo calculations, while the curves show the results of different correlated sampling runs. The right-hand panel compares variational and fixed-node Monte Carlo. The calculations are for the same system as in Figure 5.

Fixed-node Monte Carlo for a lattice Hamiltonian thus means that we choose a guiding/trial function from which we construct an effective Hamiltonian and determine its ground-state by Monte Carlo. Because of the variational property, we want to pick the Ψ_T such that E_0^{eff} is minimized; i.e., we want to optimize the trial function or, equivalently, the effective Hamiltonian. As in variational Monte Carlo we can use the concept of correlated sampling [21]. For optimizing the Gutzwiller parameter g we can even exploit the idea of rewriting the correlated sampling sums into polynomials in \tilde{g}/g . There is, however, a problem arising from the fact that the weight of a given configuration $R^{(n)}$ in iteration n is given by the product $w(R^{(n)}) = \prod_{i=1}^n m(R^{(i)}, R^{(i-1)})$: each individual normalization factor $m(R', R)$ can be written as a finite polynomial, but the order of the polynomial for $w(R^{(n)})$ keeps increasing with the number of iterations. It is therefore not practical to try to calculate the ever-increasing number of coefficients for the correlated sampling function $E^{(n)}(\tilde{g})$. But since we still can easily calculate the coefficients for the $m(R', R)$, we may use them to evaluate $E^{(n)}(\tilde{g})$ in each iteration on a set of *predefined* values \tilde{g}_i of the Gutzwiller parameter. Figure 9 shows an example. We find that the FNMC energy depends much less on the trial function than in VMC. This is not unexpected: while in variational Monte Carlo the whole trial function is fixed, only the values of the trial function next to a node enter the fixed-node Hamiltonian H_{eff} , which in FNMC is then treated exactly. To realize the higher accuracy of the FNMC method, it is nevertheless important to carefully optimize the trial function. Finally, it is interesting to note that the Gutzwiller factor that minimizes E_{VMC} is usually not quite the optimum Gutzwiller factor for fixed-node MC.

3.3 Optimization of the trial function

As mentioned before, typical trial functions for quantum Monte Carlo calculations are of the type $\Psi_T(R) = g^{D(R)} \Phi(R)$, with g the Gutzwiller parameter and Φ a Slater determinant. Along with explaining the Monte Carlo approaches, we have already described how g can be opti-

mized. The fundamental idea was that, for the reweighting in correlated sampling, only ratios of the new and old trial functions are needed so that the weights and energies appearing in the Monte Carlo calculation can be recast in the form of polynomials in the ratio of the Gutzwiller parameters. In the following, we discuss generalizations of this approach to trial functions with several Gutzwiller parameters. After that, we address the optimization of the other part of a Gutzwiller wave function: the Slater determinant. In particular, we demonstrate how the character of the Slater determinant affects the result of the Monte Carlo calculation.

3.3.1 More Gutzwiller parameters

To study the static dielectric screening [30], we have to determine the response of the charge density to the introduction of a test charge q placed on molecule i_q . To describe the test charge, the term

$$H_1(q) = qU \sum_{m\sigma} n_{i_q m\sigma} \quad (85)$$

is added to the Hamiltonian. In the spirit of the Gutzwiller ansatz, we correspondingly add a second Gutzwiller factor to the wave function that reflects the additional interaction term $qU N_{i_q}$

$$|\Psi_T(g, h)\rangle = g^D h^{N_{i_q}} |\Phi\rangle. \quad (86)$$

Finding the best Gutzwiller parameters is now a two-dimensional optimization problem. Dealing with polynomials in the two variables g and h , the method of correlated sampling works as straightforwardly as described above for the case of a plain Gutzwiller wave function. As an example, Fig. 10 shows the result of the optimization, both in variational and in fixed-node Monte Carlo, for a cluster of 64 C_{60} molecules in an fcc arrangement (periodic boundary conditions) resembling K_3C_{60} with a test charge $q = 1/4$. In practice, we first optimize the parameters in variational Monte Carlo. We then use the optimum VMC parameters as starting points for the optimization in the more time-consuming fixed-node Monte Carlo calculations.

3.3.2 Variation of the Slater determinant

In the traditional Gutzwiller ansatz, the Slater determinant Φ is the ground-state wave function of the non-interacting Hamiltonian. This is, however, not necessarily the best choice. An alternative would be to use the Slater determinant $\Phi(U)$ obtained by solving the interacting problem in the Hartree-Fock approximation. We can even interpolate between the two extremes by doing a Hartree-Fock calculation with a fictitious Hubbard interaction U_0 to obtain Slater determinants $\Phi(U_0)$. Yet another family of Slater determinants $\Phi(H_{\text{stag}})$ can be obtained from solving the non-interacting Hamiltonian with an added staggered magnetic field, which lets us control the antiferromagnetic character of the trial function. Although optimizing parameters in the Slater determinant is not possible with the method described in the preceding sections, an efficient optimization of the Gutzwiller factors makes it possible to optimize the overall trial function without too much effort.

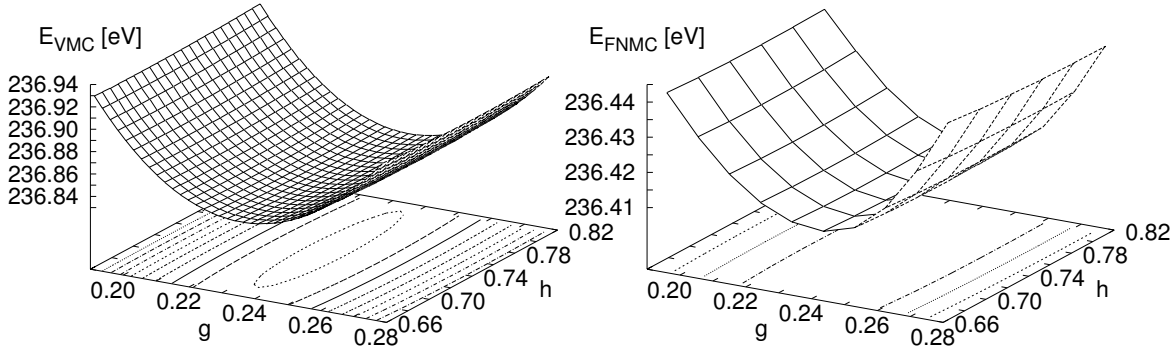


Fig. 10: Correlated sampling for the parameters g and h of the generalized Gutzwiller wave function $|\Psi_T\rangle = g^D h^{N_c} |\Phi\rangle$, in variational (left) and fixed-node Monte Carlo (right). The plots show the energy as a function of the Gutzwiller parameters g and h , both as surfaces and contours. The calculations are for an fcc cluster of 64 molecules with $96 + 96$ electrons (half-filled t_{1u} -band), an on-site Hubbard interaction $U = 1.25$ eV, and a test charge of $q = 1/4$ (in units of the electron charge).

Staggered magnetic field Introducing a staggered magnetic field, we can construct Slater determinants by solving the non-interacting Hamiltonian with an added Zeeman term. To be specific, we consider K_3C_{60} , which has a half-filled t_{1u} -band. Since K_3C_{60} crystallizes in an fcc lattice, antiferromagnetism is frustrated and the definition of a staggered magnetic field is not unique. We split the fcc lattice into two sublattices A and B such that frustration is minimized. The Zeeman term is then given by

$$H_m = H_{\text{stag}} \sum_i \text{sign}(i) [n_{i\uparrow} - n_{i\downarrow}] \quad (87)$$

with $\text{sign}(i) = +1$ if $i \in A$ and -1 if $i \in B$. It effectively introduces an on-site energy that has opposite sign for the two spin orientations on the same site, and for the same spin orientation, has opposite sign on the two sublattices. Therefore, hopping to neighboring sites on different sublattices involves an energy cost of twice the Zeeman energy. The staggered magnetic field thus not only induces antiferromagnetic order in the Slater determinant but also serves to localize the electrons. This is reflected in the fact that the optimum Gutzwiller parameter is much larger for Slater determinants constructed from a Hamiltonian with large H_{stag} than for paramagnetic Slater determinants. Varying H_{stag} then interpolates between paramagnetic/itinerant and antiferromagnetic/localized wave functions.

The energy expectation values for such trial functions as calculated in variational Monte Carlo are shown in Fig. 11. It shows E_{VMC} as a function of the antiferromagnetic correlation

$$\langle s_i s_{i+1} \rangle = \frac{1}{N} \sum_{\langle ij \rangle} (n_{i\uparrow} - n_{i\downarrow}) (n_{j\uparrow} - n_{j\downarrow}), \quad (88)$$

where the sum is over the N nearest neighbors. $\langle s_i s_{i+1} \rangle$ is a monotonic function of H_{stag} . For each different value of the Hubbard interaction U we find a curve with two minima. One

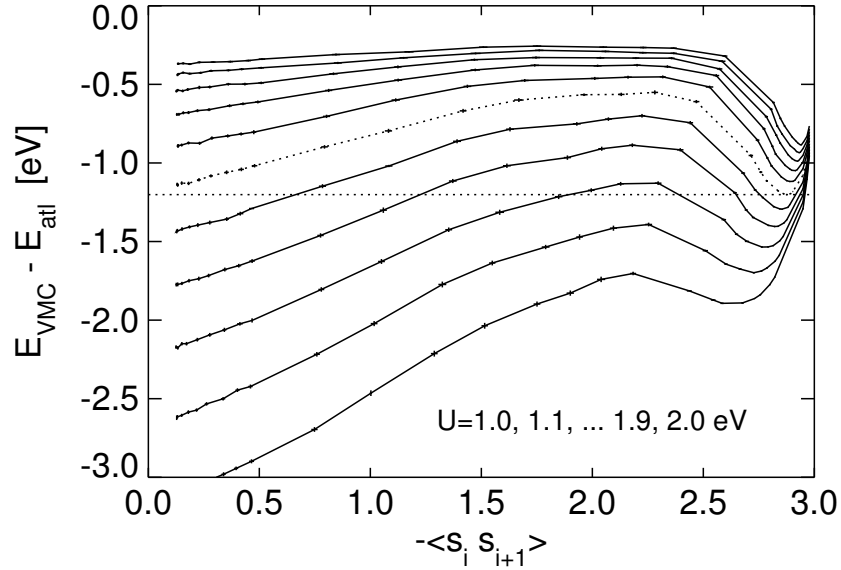


Fig. 11: Variational energy E_{VMC} for trial functions with different character. Plotted are the energies (error bars, lines are to guide the eye) for a Hamiltonian describing K_3C_{60} (periodic fcc cluster of 32 molecules) with Hubbard interaction $U = 1.0, 1.1 \dots 1.9, 2.0$ eV ($U = 1.0$ eV corresponding to the lowest curve). Instead of the total energies E_{tot} , we plot the difference of E_{tot} and the energy in the atomic limit (each site occupied by three electrons) so that the results for different U can be readily compared. The trial functions are of the Gutzwiller type. The Slater determinants were determined from diagonalizing the non-interacting Hamiltonian (i.e. setting $U = 0$) with a staggered magnetic field H_{stag} . This field gives rise to an antiferromagnetic correlation of neighboring spins, which is plotted on the abscissa. For $U = 1.5$ eV (dotted curve) the minima in the paramagnetic and the antiferromagnetic regions have about the same energy.

minimum is realized for the non-magnetic ($H_{\text{stag}} = 0$) trial function. The energy as a function of U scales roughly like $E_{\text{para}} \propto -(1 - U/U_c)^2$, as predicted by the Gutzwiller approximation. The second minimum is in the antiferromagnetic/localized region and scales roughly like $E_{\text{AF}} \propto -t^2/U$, as expected. For small U , the non-magnetic state is more favorable, while for large U the localized Slater determinant gives lower variational energies. The crossover is at $U_c \approx 1.50$ eV (dotted line) and resembles a first-order phase transition.

Hartree-Fock An alternative method for constructing Slater determinants is to use the interacting Hamiltonian with the physical Hubbard interaction U replaced by a parameter U_0 and solve it in the Hartree-Fock approximation. In practice this is done simply by means of an unrestricted self-consistent calculation for the finite, periodic clusters under consideration, starting from some charge and spin density that breaks the symmetry of the Hamiltonian. It is well known that Hartree-Fock favors the antiferromagnetic Mott insulator, predicting a Mott transition at much too small values U_c^{HF} . It is therefore not surprising that good trial functions are obtained for values of U_0 considerably smaller than U . For U_0 close to zero, the Slater determinant has metallic character, while for somewhat larger U_0 there is a metal-insulator transition. Figure 12 shows the energy as a function of U_0 for the model of K_3C_{60} . We find that the re-

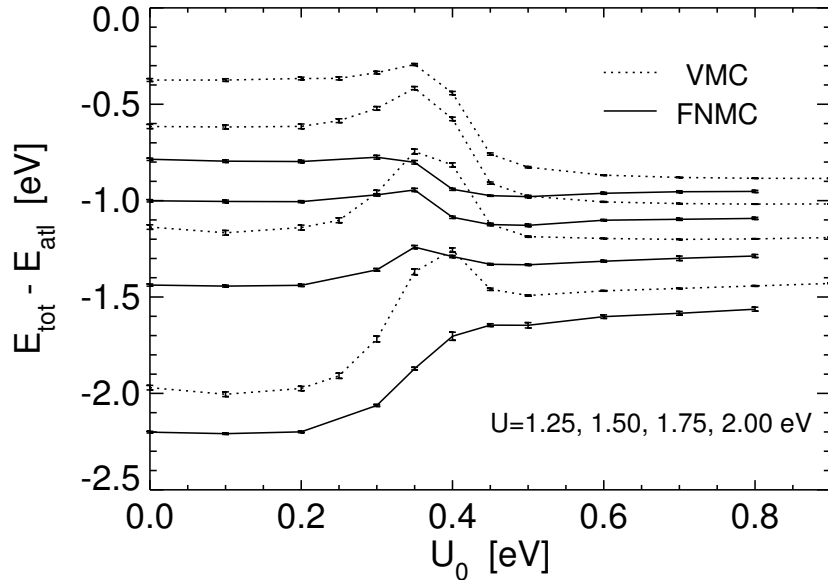


Fig. 12: *Optimizing U_0 : Dependence of variational (VMC) and fixed-node Monte Carlo (FNMC) on the trial function. U_0 is the Hubbard interaction that was used for the Slater determinant in the Gutzwiller wave function $\Psi_T(R) = g^{D(R)} \Phi(U_0)$. The Gutzwiller parameter has always been optimized. The results shown here are the energies (relative to the atomic limit) for a Hamiltonian that describes K_3C_{60} (32 molecules), with U being varied from 1.25 (lowest curve) to 2.00 eV (highest curve).*

sults of variational Monte Carlo depend quite strongly on the parameter U_0 . As expected, for a given Hubbard interaction U there is a transition from the paramagnetic region for small U_0 to a region where the trial function is antiferromagnetic. In fixed-node Monte Carlo, energies are consistently lowered and the dependence on the trial function is weaker. It seems that here it is mainly the character (paramagnetic/antiferromagnetic) of the trial function that matters. For small U , trial functions with small U_0 give lower energy, while for large U trial functions with larger U_0 are favorable. The crossover coincides with the Mott transition, which takes place between $U = 1.50$ and 1.75 eV.

3.4 Quasi-particle energies

As discussed above, the sign-problem in quantum Monte Carlo simulations for fermions makes it necessary to introduce an approximation. Such an approximation is of course undesirable when we are interested in the ground state. Surprisingly, however, we can use the fixed-node approximation to our advantage to calculate excited states and quasi-particle energies. The basic idea is that by the proper choice of the trial function, an excited state can be stabilized in the Monte Carlo simulation that otherwise would decay to a state with lower energy.

The fundamental concept for understanding this is what we call the *nodal sets*, defined as the sets of configurations where the trial function is positive/negative:

$$\mathcal{N}_\Psi^\pm := \left\{ R \mid \langle R | \Psi \rangle \gtrless 0 \right\}. \quad (89)$$

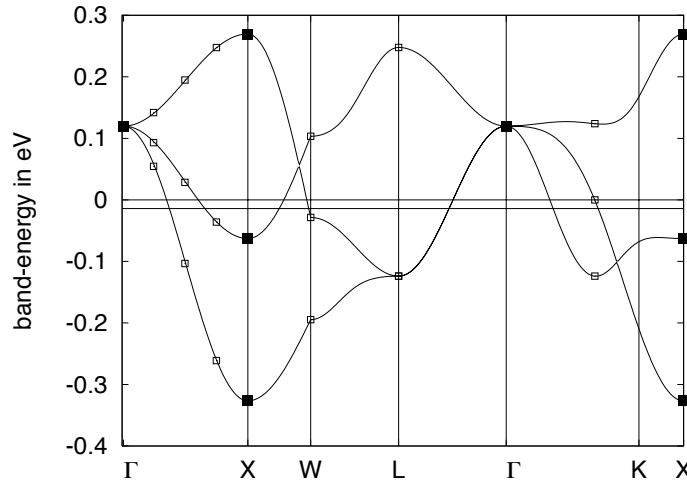


Fig. 13: C_{60} bands: Full symbols show the k -states that are present in a 4-molecule cluster with periodic boundary conditions: 3 (degenerate states) with $k = 0$ (Γ -point) and 9 states [3 band states with $k = (2\pi/a, 0, 0)$, $(0, 2\pi/a, 0)$, and $(0, 0, 2\pi/a)$] (X -point).

The first observation we make is that under the importance-sampled FNMC iterations (78) (with H replaced by H_{eff}) the nodal sets do not change. To see this, we write $|\Psi^{(n)}\rangle$ in terms of the trial function

$$\langle R|\Psi^{(n)}\rangle = \alpha^{(n)}(R) \langle R|\Psi_T\rangle. \quad (90)$$

Then the iterations (78) take the form

$$\begin{aligned} \langle \Psi_T|R'\rangle \langle R'|\Psi^{(n)}\rangle &= \sum_R G_{FN}(R', R) \langle \Psi_T|R\rangle \langle R|\Psi^{(n-1)}\rangle \\ &= \alpha^{(n)}(R') \underbrace{|\Psi_T(R')|^2}_{>0} = \sum_R \underbrace{G_{FN}(R', R)}_{\geq 0} \underbrace{|\Psi_T(R)|^2}_{>0} \alpha^{(n-1)}(R). \end{aligned}$$

Since $\alpha^{(0)}(R) = 1$ and never changes sign, $\alpha^{(n)}(R) \geq 0$ for all n .

On the other hand, each eigenstate Ψ_n of H is characterized by its nodal sets. If there were two eigenstates with the same nodal sets, then

$$\langle \Psi_n|\Psi_m\rangle = \sum_{R \in \mathcal{N}^+} \Psi_n(R) \Psi_m(R) + \sum_{R \in \mathcal{N}^-} \Psi_n(R) \Psi_m(R) > 0 \quad (91)$$

in contradiction to the orthogonality of the eigenstates.

It thus seems reasonable to try to calculate excited-state energies with fixed-node Monte Carlo, where the trial function is chosen such as to have nodal sets similar to that of the desired state. As we have seen above, the most straightforward guess for the ground-state is to use the non-interacting Slater determinant $|\Phi_0\rangle$ (remember that the Gutzwiller factors do not change the sign of the wave function). Then the simplest trial functions for the nodes of excited states are the non-interacting wave functions

- quasi-electron: $c_k^\dagger |\Phi_0\rangle$
- quasi-hole: $c_k |\Phi_0\rangle$.

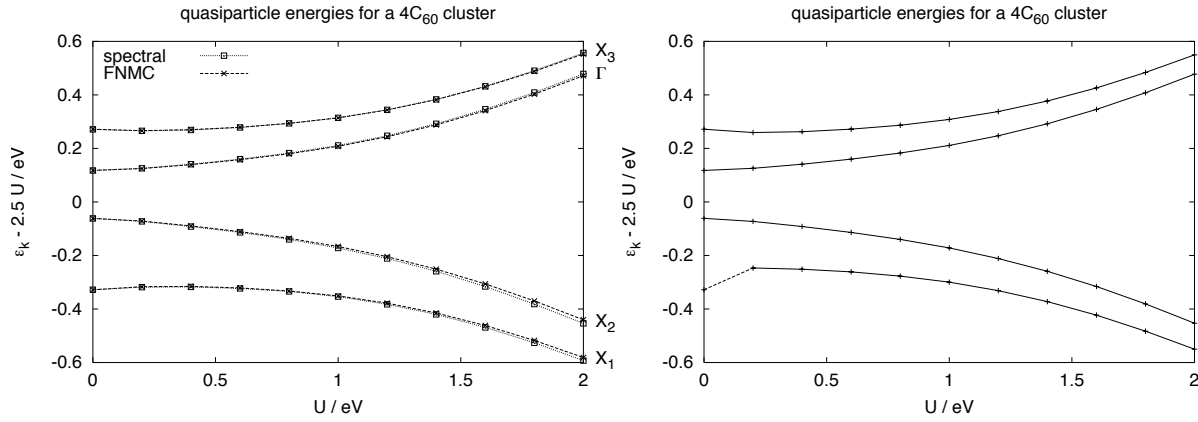


Fig. 14: *Quasi-particle energies for the half-filled, 4-molecule C_{60} cluster: The left-hand panel shows the fixed-node energies ($\varepsilon_n = E_n^{N+1} - E_0^N$ for quasi-electrons in states X_3 and Γ , $\varepsilon_n = E_0^N - E_n^{N-1}$ for quasi-holes in X_1 and X_2). For comparison, the open squares give the position of the peak in the corresponding spectral function calculated by exact diagonalization, as shown in Figure 15. The right-hand panel shows the result of Lanczos calculations starting from the quasi-particle trial functions used in fixed-node Monte Carlo. It is clear that for $U > 0$ the quasi-hole at X_1 is not stable.*

To see how this simple approach works, we consider the model for describing the t_{1u} -electrons in C_{60} (cf. Table 1) and compare to results of exact diagonalization for a cluster of 4 molecules. The t_{1u} -bands are reproduced in Figure 13, where the filled squares represent the reciprocal lattice vectors of the 4-molecule simulation cell: three degenerate states at the Γ point, and three different levels at the X point, each of which is three-fold degenerate. For the half-filled system, the lower two levels at the X point are filled (below we will refer to them as X_1 and X_2), while the highest level at X (referred to as X_3) and Γ are empty. To calculate the quasi-particle energies, we first perform a calculation for the ground-state energy of the half-filled system E_0^N using a Gutzwiller wave function based on the non-interacting Slater determinant $|\Phi_0\rangle$. Then, we calculate the fixed-node energy for the system with an extra electron/hole with a trial function based on $c_k^\dagger |\Phi_0\rangle$ or $c_k |\Phi_0\rangle$, respectively. To keep the wave functions real we make use of the inversion symmetry, setting $c_k = \cos(k r_i) c_i$. The resulting quasi-particle energies are plotted in Figure 14. To compare to the true quasi-particle energies, we have calculated the corresponding spectral functions

$$A(\mathbf{k}, \omega) = \begin{cases} \sum_n \left| \langle \Psi_n^{N+1} | c_k^\dagger | \Psi_0^N \rangle \right|^2 \delta(\omega - (E_n^{N+1} - E_0^N)) & \text{(quasi-electron)} \\ \sum_n \left| \langle \Psi_n^{N-1} | c_k | \Psi_0^N \rangle \right|^2 \delta(\omega - (E_0^N - E_n^{N-1})) & \text{(quasi-hole)} \end{cases}$$

by exact diagonalization (see Figure 15). The position of the peak in $A(\mathbf{k}, \omega)$ is plotted in Figure 14. We find a remarkable agreement between fixed-node and exact energies. This is not too unexpected. Looking again at the band-structure, we see that the quasi-electron at X_3 is the lowest energy state with that k -vector, while the quasi-electron at Γ is the lowest with $k = 0$. So these states are ground-states in their respective symmetry sectors and should thus be accessible by a ground-state method like fixed-node Monte Carlo. The same is true for the quasi-hole at

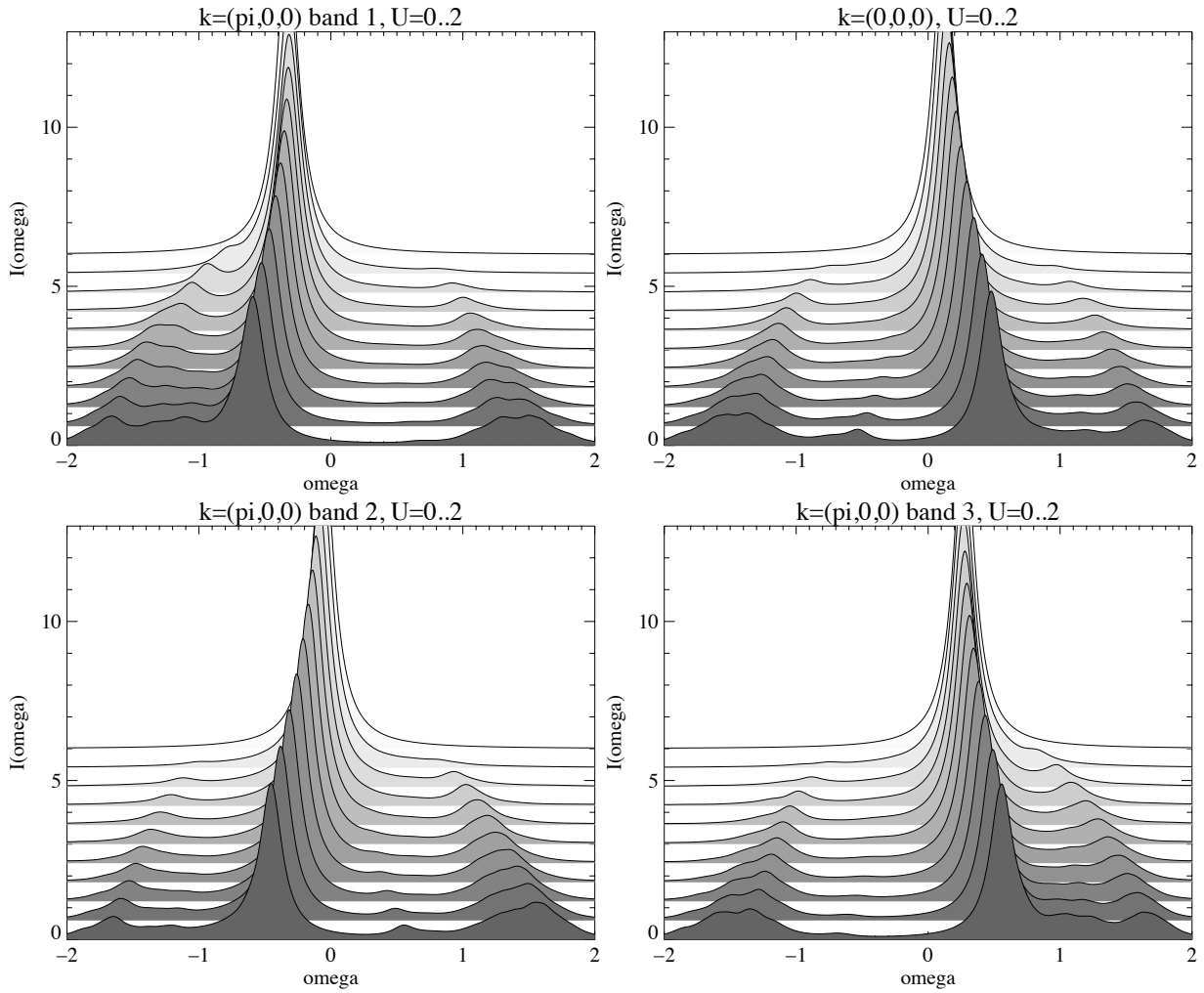


Fig. 15: Spectral function for a 4 C_{60} molecule cluster calculated by exact diagonalization. From back to front the curves show the spectral function for U from 0 to 2 eV in steps of 0.2 eV.

X_2 . The quasi-hole at X_1 , however, has the same k as the one at X_2 and thus cannot be the ground-state in that symmetry sector. To check this, we have performed Lanczos runs starting from the determinants used in the respective fixed-node calculations. The results are shown in the right panel of Figure 14. We indeed find that all states are stable, except for X_1 , which for $U > 0$ decays into a lower-energy quasi-hole. This decay is induced by the interaction term. This can be understood by writing it in k -space

$$\frac{U}{M} \sum_{k,k',q} c_{k\uparrow}^\dagger c_{k-q}^\dagger c_{k'\downarrow}^\dagger c_{k'+q\downarrow} .$$

What happens for the X_1 state is visualized in Figure 16: The lower-energy quasi-hole is obtained by filling the X_1 hole with an X_2 electron, while exciting another X_2 electron into Γ .

To verify that this picture is indeed correct, we have calculated the spectral function for the decayed state

$$A = \sum \left| \langle \Psi_n^{N-1} | c_{X_2}^\dagger c_\Gamma^\dagger c_{X_2} | \Psi_0^N \rangle \right|^2 \delta(\omega - (E_0^N - E_n^{N-1})) , \quad (92)$$

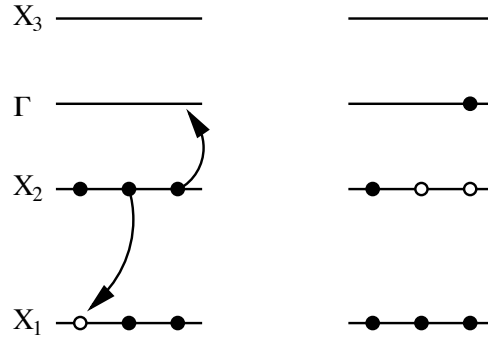


Fig. 16: *Quasi-particle decay induced by interaction term for a quasi-hole at X_1 . Both states have the same k , so the transition is allowed by symmetry. (Notice that there are three different X -points in the three different directions. Choosing appropriate directions for the quasi-holes, the momentum for the original and decayed state are the same, up to a reciprocal lattice vector.)*

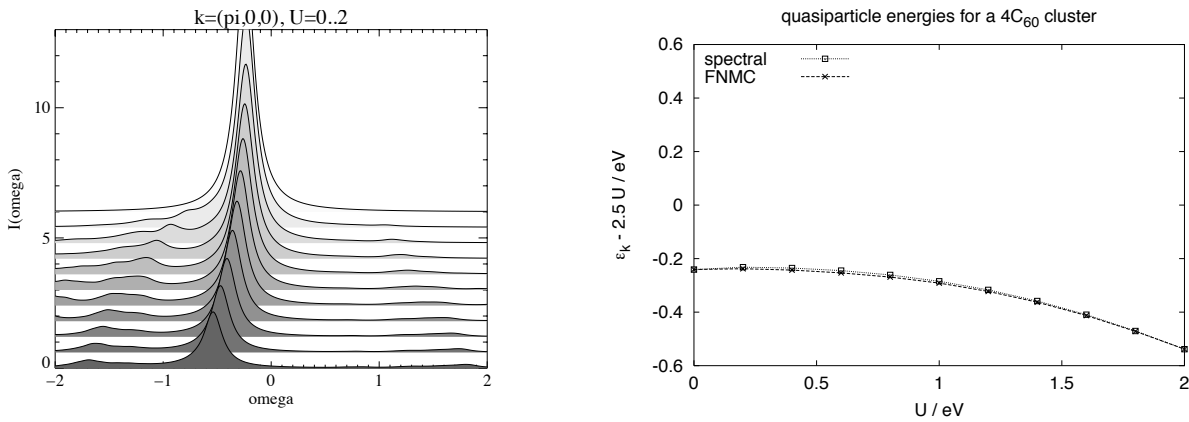


Fig. 17: *Three-body quasi-hole $c_{X_2} c_{\Gamma}^{\dagger} c_{X_2}$: spectral function and fixed-node energies.*

shown in Figure 17. As expected, the position of the peak corresponds closely to the energy of the decayed state found in the Lanczos calculation of Figure 14. Moreover, performing a fixed-node calculation with the trial function $c_{X_2} c_{\Gamma}^{\dagger} c_{X_2} |\Phi_0\rangle$ again gives excellent agreement with the exact quasi-particle energy (see right panel of Figure 17). Working with such more complex quasi-particles, we could extract quasi-particle interactions. A more straightforward application is to look at how the quasi-particle dispersion changes with U , as shown in Figure 18. This can be related to the effective mass m^* defined as

$$\frac{k_F}{m^*} = \left. \frac{d\varepsilon_k}{dk} \right|_{k_F}. \quad (93)$$

Rewriting the derivative as a finite difference, for the ratio of the effective mass to the bare mass at $U = 0$ we obtain

$$\frac{m^*}{m_0} \approx \frac{\Delta\varepsilon_0}{\Delta\varepsilon}. \quad (94)$$

The ratio on the right-hand side is also plotted in Figure 18. Even though the k -points for the four molecule cluster are quite far apart, so that the finite difference is not a good approximation to the derivative, we get consistent results when comparing the results derived from the quasi-electron and the quasi-hole states.

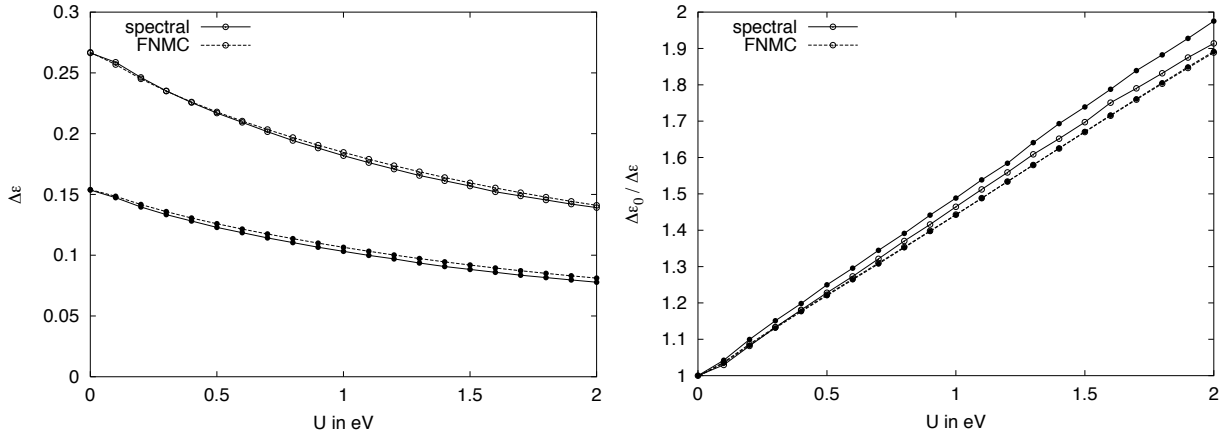


Fig. 18: Change in quasi-particle dispersion with U . The left-hand panel shows the energy difference between the two quasi-electron (filled circles) and the two simple quasi-hole (open circles) states. The full line connects the exact results, the full dashed line the fixed-node results. The right-hand panel shows the inverse of the energy difference normalized by its value at $U = 0$.

4 Conclusion

Practical many-body calculations need to be done on finite systems. A standard approach for reducing a solid to a finite system is to introduce periodic boundary conditions on finite clusters. How well such a periodic cluster represents the infinite solid depends on its shape. We have seen how we can use the Hermite normal form to systematically enumerate all distinct clusters. Introducing more general twisted boundary conditions, we can study the dependence of the system on the boundary conditions, providing an elegant criterion for distinguishing metals from (Mott) insulators.

We have demonstrated how to use the local energy to derive compact variational wave functions that incorporate a correlation-hole based on the cusp conditions. In contrast to a CI-expansion, such Jastrow/Gutzwiller functions need only few parameters to efficiently describe correlation effects. Still, simple correlation factors are usually not sufficient to describe a metal-insulator transition. To improve on the wave function, we can use projection techniques. In principle, they converge to the ground state, in practice their stochastic implementation is, however, hampered by the appearance of negative matrix elements – the fermion sign problem. The fixed-node approximation is a practical way for eliminating the sign problem without compromising accuracy. Moreover, fixing the nodes can be used to stabilize quasiparticle states.

Acknowledgment

Support of the Deutsche Forschungsgemeinschaft through FOR1346 is gratefully acknowledged.

References

- [1] E. Koch: *Many-body states*, in [33]
- [2] A. Szabo and N.S. Ostlund: *Modern Quantum Chemistry* (Dover Publications, 1996)
- [3] M. Born and T. von Kármán, *Physikal. Z.* **13**, 297 (1912)
- [4] W.M.C. Foulkes, L. Mitas, R.J. Needs, and G. Rajagopal, *Rev. Mod. Phys.* **73**, 33 (2001)
- [5] E. Wigner, *Phys. Rev.* **46**, 1002 (1934)
- [6] W. Kohn, *Phys. Rev.* **133**, A171 (1964)
- [7] M. Newman: *Integral Matrices* (Academic Press, New York, 1972)
- [8] H. Cohen: *A Course in Computational Algebraic Number Theory* (Springer, Heidelberg, 1993)
- [9] D.D. Betts, H.Q. Lin, and J.S. Flynn, *Can. J. Phys.* **77**, 353 (1999)
- [10] H.J. Monkhorst and J.D. Pack, *Phys. Rev. B* **13**, 5188 (1976)
- [11] E. Koch: *The Lanczos Method*, in [31]
- [12] T. Kato, *Commun. Pure Appl. Math.* **10**, 151 (1957)
- [13] B.L. Hammond, W.A. Lester, P.J. Reynolds:
Monte Carlo Methods in Ab Initio Quantum Chemistry (World Scientific, 1994)
- [14] R. Jastrow, *Phys. Rev.* **98**, 1479 (1955)
- [15] S. Fahy, X.W. Wang, and S.G. Louie, *Phys. Rev. B* **42**, 3502 (1990)
- [16] E. Pavarini and E. Koch: *Introduction*, in [31]
- [17] M.C. Gutzwiller, *Phys. Rev.* **137**, A1726 (1965)
- [18] J. Bünenmann: *The Gutzwiller Density Functional Theory* in [32]
- [19] D.M. Ceperley, G.V. Chester, and M.H. Kalos, *Phys. Rev. B* **16**, 3081 (1977)
- [20] P. Horsch and T.A. Kaplan, *J. Phys. C* **16**, L1203 (1983);
H. Yokoyama and H. Shiba, *J. Phys. Soc. Jpn.* **56**, 1490 (1987)
- [21] E. Koch, O. Gunnarsson, and R.M. Martin, *Phys. Rev. B* **59**, 15632 (1999)
- [22] C. Umrigar, K. Wilson, and J. Wilkins, *Phys. Rev. Lett.* **60**, 1719 (1988)
- [23] E. Koch, O. Gunnarsson, and R.M. Martin, *Phys. Rev. B* **60**, 15714 (1999)

- [24] D. Vollhardt, *Rev. Mod. Phys.* **56**, 99 (1984)
- [25] W.F. Brinkman and T.M. Rice, *Phys. Rev. B* **2**, 4302 (1970);
T.M. Rice and W.F. Brinkman, in *Critical Phenomena in Alloys, Magnets, and Superconductors*, ed. by R.E. Mills, E. Ascher, R. Jaffee (McGraw Hill, New York, 1971)
- [26] W. Metzner and D. Vollhardt, *Phys. Rev. Lett.* **59**, 121 (1987)
and *Phys. Rev. B* **37**, 7382 (1988)
- [27] A.J. Millis and S.N. Coppersmith, *Phys. Rev. B* **43**, 13770 (1991)
- [28] N. Trivedi and D.M. Ceperley, *Phys. Rev. B* **40**, 2737 (1989)
- [29] D.F.B. ten Haaf, H.J.M. van Bemmelen, J.M.J. van Leeuwen, and W. van Saarloos,
Phys. Rev. Lett. **72**, 2442 (1994) and D.F.B. ten Haaf, H.J.M. van Bemmelen,
J.M.J. van Leeuwen, W. van Saarloos, and D.M. Ceperley, *Phys. Rev. B* **51**, 13039 (1995)
- [30] E. Koch, O. Gunnarsson, and R.M. Martin, *Phys. Rev. Lett.* **83**, 620 (1999)
- [31] E. Pavarini, E. Koch, D. Vollhardt, and A. Lichtenstein (eds.):
The LDA+DMFT approach to strongly correlated materials
Reihe Modeling and Simulation, Vol. 1 (Forschungszentrum Jülich, 2011)
<http://www.cond-mat.de/events/correl11>
- [32] E. Pavarini, E. Koch, F. Anders, and M. Jarrell (eds.):
Correlated Electrons: From Models to Materials
Reihe Modeling and Simulation, Vol. 2 (Forschungszentrum Jülich, 2012)
<http://www.cond-mat.de/events/correl12>
- [33] E. Pavarini, E. Koch, and U. Schollwöck (eds.):
Emergent Phenomena in Correlated matter
Reihe Modeling and Simulation, Vol. 3 (Forschungszentrum Jülich, 2013)
<http://www.cond-mat.de/events/correl13>